Ultrafast Readout of Representations from Spatially Distributed Rodent Hippocampal Field Potentials

Liang Cao[1,2], Viktor Varga[1], and Zhe S. Chen[1,4,*]

[1]The Neuroscience Institute, New York University School of Medicine, New York, NY 10016, USA.
[2]Department of Physics, East China Normal University, Shanghai, China.
[3]Center for Neural Science, New York University, New York, NY 10016, USA.
[4]Department of Psychiatry, Department of Neuroscience and Physiology, New York University School of Medicine, New York, NY 10016, USA.
*** Correspondence: zhe.chen@nyulangone.org (Z.S.C.)**

SUMMARY

Demodulated oscillatory activity at theta frequency band extracted from spatially distributed hippocampal local field potentials (LFPs) encode rodent's position during maze run. However, it remains unclear how spatial information is encoded in hippocampal field potentials across various immobility and sleep states. Here, we showed that unclustered hippocampal field potential amplitude at ultra-high frequency band (>300 Hz), or known as multiunit activity (MUA), across high-density silicon probe channels provide not only a fast and reliable reconstruction of the rodent's position in wake, but also a direct readout of replay content during sharp wave ripples (SPW-Rs) in immobility and slow wave sleep. We also employed unsupervised learning approaches to extract low-dimensional MUA features during run and ripple periods, and developed Bayesian methods to infer latent dynamical structures from lower-rank MUA features that were coherent with those derived from clustered spikes. Furthermore, we used an optical flow estimation method to identify propagating spatiotemporal LFP patterns, and derived a set of hippocampal LFP spatiotemporal features for decoding applications. Finally, we developed hybrid forward decoding strategies to predict animal's future decision at a choice point in goal-directed navigation. Our results point to a robust real-time decoding strategy from large-scale (up to 100,000 electrodes) recordings for closed-loop neuroscience experiments.

INTRODUCTION

Cutting-edge large-scale high-density electrode arrays have enabled us to record spatially distributed neural activity within local or multiple brain circuits (Berenyi et al., 2014; Jun et al. 2017; Chung et al., 2019), yet it remains challenging to reliably uncover representations of spatiotemporal neural activity. The hippocampus contributes to a wide range of brain functions responsible for spatial and episodic memories, learning and planning (Pfeiffer and Foster, 2013). Population spike activities from hippocampal place cell assemblies provide a readout of the rat's spatial location (Zhang et al., 1998; Davidson et al. 2009; Kloosterman et al. 2014; Grosmark and Buzsaki, 2016; Hu et al. 2018; Ciliberti et al. 2018). However, direct use of spike information for neural decoding remains challenging due to practical issues of spike sorting and unit instability, let alone the prohibitive computational cost in the era of big data (Rey et al., 2015; Rossant et al., 2016; Carlson and Carin, 2019). In contrast, hippocampal field potentials consist of collective local subthreshold activities around the recording site, serving as an alternative information carrier for spatial representation (Buzsaki et al. 2012; Agarwal et al. 2014). On the other hand, advances in neurotechnology on electrode arrays have enabled us to record large-scale field potentials from human brain (Khodagholy et al., 2015; Chang, 2015; Zhang and Jacobs, 2015). Developing effective statistical methods for uncovering neural representations of these signals during memory tasks or sleep remains a central goal in computational neuroscience.

Hippocampal sharp-wave ripples (SPW-Rs) are important hallmarks for memory reactivations during immobility and non-rapid-eye-movement (NREM) sleep (Roumis and Frank, 2015; Buzsaki, 2015; Fernandez-Ruiz et al. 2015). Decoding the content of hippocampal replays during ripple events can help dissect circuit mechanisms of memory consolidation, planning and decision-making (Davidson et al., 2009; Pfeiffer and Foster, 2013; Foster, 2017; Olafsdottir et al., 2018). Evidence has suggested that hippocampal LFPs may encode neuronal ensemble activations during SPW-Rs (Taxidis et al. 2015), but it remains unknown how the information embedded in field potentials contribute to spatial representations, and how these spatially distributed LFP representations relate to ensemble spike representations at different brain states.

To address these questions and challenges, here we systematically investigate large-scale multi-site recorded rodent hippocampal field potentials and the spatial representation power during maze running, memory replay decoding, and spatial decision-making. We propose and develop a set of independent and complementary hippocampal field potential-derived features, and develop innovative supervised or unsupervised learning methods while validating them in various applications. Without the need of spike sorting, these spatiotemporal features not only provide direct and robust solutions to decoding and prediction problems, but also open new opportunities for exploratory neural data visualization or finding latent structures in the absence of behavioral measure.

RESULTS

Spatially Distributed Hippocampal Field Potentials Encode Position in Maze Run

Rats and mice were implanted with high-density silicon probes (varying from 64 to 512 channels; see **Table S1**) in the dorsal hippocampus or hippocampi while freely foraging in a circular track, linear track, T-maze or open field environment (**Figure S1A**). We processed the extracellular raw voltage traces of hippocampal recordings and extracted independent neural signals at different frequency bands (**Figure 1A**). During run epochs, we found that both demodulated theta (4-12 Hz) activity—or in short LFP_θ (amplitude or phase or both, Agarwal et al. 2014) and the instantaneous LFP amplitude at ultra-high frequency (>300 Hz) band---also referred to as MUA (Stark and Abeles, 2007; Bansal et al., 2012 Smith et al., 2013), recorded from multiple recording sites could be used to reliably decode animal's position (**Figures 1B,C** and **S1B**). Augmenting multiple LFP-based features, such as combining LFP_θ or MUA with their own activity history (**Figure 1C**) or combining MUA with LFP_θ (**Figure S1B**), further improved the decoding accuracy. We systematically assessed the decoding performance using instantaneous LFP amplitude features at various frequency bands and temporal bin sizes and found that >300 Hz band was most effective. In temporal windows of <300 ms the various LFP and spike features and their combinations were comparable, whereas at longer time intervals coding errors increased more rapidly from LFP_θ than for spike-containing combinations (**Figure S2**).

Spatial coverage of the hippocampal place fields are crucial to the decoding accuracy in a larger environment. In the open field, we found that 64-channel joint LFP-based features yielded better decoding accuracy than clustered spike-based decoding (Dataset 5; mean±SD median error: 10.81±0.25 cm for spikes and 8.85±0.21 cm for LFPs; rank-sum test, $P=1.95\times10^{-21}$; **Figures 1D** and **1E**; see also **Movie S1**), possibly because decoding 2D environments requires a large number of isolated units (Wilson and McNaughton, 1983).

It is noted that the >300 Hz LFP signal also contains spike activity (Zano et al. 2011; Buzsaki et al., 2012; Waldert et al. 2013). To remove the contamination of spike activity, we decomposed the broadband LFP signal into non-spiking (by removing detected spikes) and 'soft' spiking components (by retaining only detected spikes; **Figure 1F**). Following down-sampling (1,250 Hz) and high-pass filtering (>300 Hz) operations (**Figure 1G**), and repeating decoding analyses showed that MUA features produced the best decoding accuracy (**Figure 1H**), suggesting that the position decoding contribution of >300 Hz amplitude was mainly derived from the clustered spiking-related activity, although decoding the animal's position does not require a preprocessed clustering step.

Since spiking activity is derived mainly from the somatic layer, we further examined the impact of anatomical location of recording electrodes on decoding performance (**Figure S3**; Dataset 3). As expected, recording sites in the CA1 and CA3 pyramidal layers contributed most to overall MUA decoding accuracy. Interestingly, because these two layers are known to have higher cell density.

High-Frequency Band Hippocampal MUA Features Decode Replay Events

During immobility and NREM sleep, putative hippocampal memory replay events occur during SPW-Rs, where population firing bursts coincide with a high ripple band amplitude (**Figure 2A**). A central task of statistical analysis is to identify the content of these replay contents and assess

their significance in the absence of behavioral ground truth. Remarkably, we found that these unclustered, spatially distributed MUA features also encoded the replay content during ripple events (**Figure 2B**). Remarkably, the linear decoder estimated from maze run (based on sparse Bayesian linear regression; Methods) could be directly transferred to ripple periods, with similar reconstruction of memory replays as the results derived from clustered spikes (**Figures 2C** and **S4A**). In addition, MUA and clustered spike-based decoding strategies produced slightly different statistics for significant memory replay events (**Figures 2D** and **S4B**), suggesting that these two decoding strategies are complementary.

Unsupervised Learning Reveals Consistent Representations between Low-Rank Structures of Hippocampal MUA with Spikes of Neuronal Ensembles

Establishing a mapping between animal's position and neural activity requires training samples during maze run. However, from an internal brain observer perspective, it is important for downstream structures of the hippocampus to quickly infer spatial representations without direct behavioral measures. We employed two latent variable models and unsupervised learning methods, nonnegative matrix factorization (NMF) and reconstruction independent component analysis (RICA), to extract lower-rank features from multi-site recorded hippocampal MUA (Methods; **Figures 3A** and **3B**). Position-averaging on the feature matrix derived from NMF or RICA revealed localized structures in the latent state space. From the lower-rank MUA features (derived from NMF or RICA, followed by feature resampling; see Methods and **Figure S5**), we further trained an unsupervised Bayesian hidden Markov model (HMM) (Linderman et al., 2016) and inferred the latent state trajectories (**Figure 3C**). During run, the lower-rank MUA-inferred state trajectories matched well with the animal's position as well as spike-inferred state trajectories (**Figure 3D**). During ripples, we also observed similar correspondence between two latent state trajectories derived independently from lower-rank MUA features and clustered spikes (**Figure 3E**). In both maze run and ripple events, the preprocessed lower-rank feature extraction was critical for learning the latent state trajectories; direct use of LFP or MUA features alone yield poor performance.

Furthermore, projecting high-dimensional MUA features onto a 2D embedding space revealed coherent structures in agreement with the animal's position or spatial topology of the environment (**Figure S6**). Together, these results confirmed that unsupervised learning methods can uncover neural representations of large-scale hippocampal LFP signals without *a priori* measurement of animal's behavior, which has been a challenge for inferring memory replays of hippocampal nonspatial representations or hippocampal-neocortical representations during sleep (Allen et al., 2016; Chen et al. 2016; Chen and Wilson, 2017; Maboudi et al., 2018).

Independent, Parallel and Complementary Hippocampal LFP Spatiotemporal Patterns for Spatial Representation

Propagating waves in the rat hippocampus have been reported at the theta and ripple frequency bands (Lubenov and Siapas, 2009; Patel et al. 2012, 2013; Agawal et al., 2014). Next, we investigated how these spatiotemporal patterns across multi-site LFP channels were coordinated

in space and time. We mapped the bandpass-filtered LFP signals (at 4-12 Hz or >300 Hz band) onto the 2D electrode space in time to obtain a video sequence (frame rate: 10 Hz), and then employed an optical flow estimation approach to compute the vector field between two consecutive image frames (Methods; **Figure 4A**). The spatiotemporally local optical flow revealed position-tuned wave patterns in the MUA or other LFP-derived features. Therefore, the optical flow method can help reveal the intrinsic propagating wave characteristic of band-limited signals (beyond theta and ultra-high frequency bands).

In addition to exploratory data visualization, we further investigated whether the high-dimensional optical flow features were useful for decoding. Remarkably, these spatiotemporal patterns estimated directly from bandpass-filtered LFP signals provided sufficient information for reconstructing animal's position (LFP_θ-flow in **Figure 4B**; see also **Figure S7** and **Movie S2**). In fact, we discovered that a set of field potential-derived spatiotemporal patterns (**Figure 4C**) contained complementary information for position decoding (**Figure 4D** for Dataset 3; **Figure S7C** for Dataset 1). The variability in contributions of individual LFP features in different datasets might be ascribed to spatial sampling or different layout in the implanted probes (**Figure S1C**). Together, these hippocampal LFP spatiotemporal features or their combinations provide a rich repertoire for position decoding across brain states (**Table 1**).

Hybrid Decoding Strategy for Predicting Goal-Directed Navigation Behavior

Hippocampal place cells exhibit trajectory-dependent or prospective/retrospective memory coding in spatial navigation (Frank et al., 2000; Ferbinteanu and Shapiro, 2003; Ji and Wilson, 2008). Here we investigated if a prospective decoding strategy based on hippocampal LFP features could predict animal's decision in a spatial alternating task (Dataset 6). We adapted the standard decoding strategy and attempted to predict animal's prospective L/R arm position while the animal ran in the central arm towards the choice point, with forward time lag ranging from 0.5 s to 0.15 s (5-15 temporal bins; **Figure 5A**). Remarkably, both hippocampal spikes and joint (LFP_θ+MUA) features (**Figures 5B** and **S8**) carried predictive representations of upcoming maze locations in the L/R arm. We found that the prediction accuracy in prospective coding improved as animals moved closer to the choice point, where the predictability was far beyond the chance level (see shuffled statistics in **Figure S8**). In two tested animals, the joint features achieved a high (~90%) prediction accuracy in correct trials (n=4 sessions for each mouse; see **Figure S8** for incorrect trials).

In another independent test, we further trained a linear support vector machine (SVM) classifier to predict the L/R decision (for correct trials only) by pooling LFP_θ and MUA features at consecutive 5 temporal bins prior to the choice point (Methods and **Figure 5C**). The cross-validation classification accuracy and trend was also comparable to **Figure 5B** in two tested animals (correct trials: 72-98% for spikes, 62-95% for joint (LFP_θ+MUA) features; incorrect trials: 62-92% for spikes, 56-85% for joint features). The gradual decay in classification accuracy away from the choice point was partially due to the increased trial variability in the animal's actual position because of the variability in run speed. Notably, the degraded accuracy trend remained

consistent between forward and backward direction, when triggering temporal bins from either the end ('backward') or start ('forward') position of the central arm (**Figure S9**).

Real-Time Decoding Strategy for Large-Scale Hippocampal Recordings

Our results directly point to an efficient hippocampal MUA or LFP_θ-based decoding strategy with two key advantages: easy circuit implementation (linear mapping), as well as the stability and longevity of LFP signals (in contrast to unreliable spike detection and sorting of unstable units). First, we validated the robustness of MUA or LFP_θ-based decoding strategy. In multiple consecutive recording sessions (separated by days in between) from the same animal and the same environment (Dataset 6), we trained the linear decoder using one run session and tested it on remaining run sessions. Remarkably, the MUA and LFP_θ decoding strategies produced outstanding performance across several consecutive run sessions/days (**Figure 6A**). Furthermore, we assessed the average cross-session decoding performance when training and testing sessions were separated by different intervals, and found a V-shaped performance drop with increasing time intervals (**Figure 6B**). When the intervals between training and testing session was short, MUA features produced better decoding performance; yet the performance of LFP_θ features decayed slower. While MUA and LFP_θ features were complementary, combining them further improved the decoding accuracy. The slowly degraded decoding accuracy in these features across days might be induced by neuroplasticity and place cell remapping (Frank et al., 2004).

Furthermore, we ran computer simulations to test the scalability of hippocampal MUA decoding algorithm. Running an optimized C/C++ code on a multi-core desktop computer, the readout could accommodate a real-time speed at a scale up to hundreds of thousands of (>100,000) recording channels during both wake and sleep (**Figure 6C**). Next, it is important to assess the statistical significance of online decoded replay events. We adapted a real-time spike-based replay assessment strategy (Hu et al., 2018) to accommodate MUA decoding (Methods). By presetting the pseudorandom shuffle operations (n=2,000 shuffles), we could accommodate a real-time speed (<20 ms) for both decoding and significance assessment for 128 channels in a 1D environment (**Figure 6D**), with comparable results derived from off-line significance assessment (**Table S3**).

DISCUSSION

Rodent hippocampal clustered spikes and spatially distributed theta waves are known to encode animal's position. Here, we further demonstrated that unclustered hippocampal spatiotemporal patterns at different frequency bands contain rich spatial representations in wake and sleep. Based on high-density electrophysical recordings of the rodent hippocampus, we proposed a set of spatiotemporal features of hippocampal field potentials and developed efficient statistical decoding methods for ultrafast readout of spatial representations. The decoding performance derived from each feature depends heavily on the layout of the silicon probe and the implanted location of hippocampus layer.

The instantaneous readout of multi-site hippocampal field potentials provides a plausible mechanism of information integration along the septotemporal axis of the hippocampus, forming the traveling waves (Lubenov and Siapas, 2009; Patel et al. 2012, 2013). Such traveling waves can also propagate the coded information to the downstream structures of the hippocampus. Our results on MUA decoding were also consistent with our previous finding that unsorted hippocampal ensemble spikes can reliably encode rodent's position (Kloosterman et al. 2014; Deng et al., 2015; Hu et al. 2018). We have also demonstrated that MUA decoding strategies are robust and reliable to predict animal's decision-making in goal-directed navigation. The most computationally efficient MUA decoding strategy is particularly useful for content-based real-time closed-loop circuit manipulation in rodents with chronic implant, which may prove critical for causal circuit dissection of hippocampal-prefrontal coordination in decision-making (Singer et al., 2013; Schmidt et al., 2019). Efficient sampling, processing and transmission of band-limited signals make it ideal for wireless-empowered implanted devices.

A central task in computational neuroscience is to link neural representations with animal's behavior or internal cognitive state. Therefore, development of unsupervised machine learning methods is important for discovering intrinsic latent structures of high-dimensional spatiotemporal neural data, especially in the absence of behavioral measures (Cunningham and Yu, 2014; Chen et al., 2014; Linderman et al., 2016; Townsend and Gong, 2018; Chaudhuri et al., 2019). Since high-density LFP recordings produce a high degree of input correlation between neighboring channels, low-rank feature extraction or dimensionality reduction (e.g., ICA, NMF and embedding) can help exploratory data visualization and subsequent decoding analysis.

Hippocampal spatiotemporal patterns often display in the form of traveling wave (Lubenov and Siapas, 2009; Patel et al. 2012, 2013) or sequential structure ('hippocampal sequences') in space and time during various behavioral states (Buzsaki and Tingley, 2018). In addition to ripple sequences, hippocampal theta sequences have been known to encode look-ahead trajectories or current goals in planning (Foster and Wilson, 2008; Gupta et al., 2012; Wikenheiser and Redish, 2015). Furthermore, internally-generated sequences may predict animal's choices in a memory task or guide navigation when external spatial cues are reduced (Pastakova et al., 2008; Wang et al., 2015; Villette et al., 2015). To date, rodent hippocampal memory replays have been widely studied in NREM sleep. During REM sleep, rodent hippocampal LFP theta oscillations are pronounced, yet their spatiotemporal patterns are less well understood (Louie and Wilson, 2001). Our LFP-based features and decoding methods proposed here may provide new opportunities to investigate these REM sleep-associated spatiotemporal patterns.

Although we only investigated the rodent hippocampal circuit here, our 'place' decoding analysis and methods can be readily applied to other neocortical areas that encode similar spatial information, such as the entorhinal cortex, primary visual cortex, retrosplenial cortex, parietal cortex and somatosensory cortex (Hafting et al., 2015; Whitlock et al., 2008; Mao et al., 2017; Ji and Wilson, 2007; Haggerty and Ji, 2015; Hu et al., 2018; Long and Zhang, 2019). Examination of the coordinated representations of large-scale hippocampal-neocortical spatiotemporal activity during various behavioral states would help dissect the mechanisms of memory, learning, planning and decision-making (Chung et al., 2019).

Finally, the superior representational power of hippocampal field potentials points to potential applications for investigating human memory replays based on high-density MEG or EEG recordings (Kurth-Nileson et al. 2016; Liu et al., 2019; Huang et al. 2018), or for predicting human hippocampal memory task outcomes based on ECoG recordings (Zhang and Jacobs, 2015).

STAR METHODS

Detailed methods are provided in the online version of this paper and include the following:

- KEY RESOURCE TABLE
- CONTACT FOR REAGENT AND RESOURCE SHARING
- EXPERIMENTAL MODEL AND SUBJECT DETAILS
- METHOD DETAILS
    - Data preprocessing and analysis
    - Multichannel LFP feature extraction
    - Decoding analysis
    - Real-time decoding
- QUANTIFICATION AND STATISTICAL ANALYSIS
    - Statistical assessment of decoding
    - Region-specific assessment of decoding
- DATA AND SOFTWARE AVAILABILITY

SUPPLEMENTAL INFORMATION

Supplemental information includes ten figures, three tables, and three movies.

AUTHOR CONTRIBUTIONS

Z.S.C. and L.C. conceived this research and designed the experiments; L.C. and Z.S.C. analyzed the data; V.V. performed the mouse experiments; Z.S.C. wrote the paper; and all authors participated in the editing and revisions of the manuscript.

ACKNOWLEDGMENTS

We thank G. Agarwal and I.H. Stevenson for valuable discussions. We also thank the valuable feedback and support of G. Buzsaki and the Buzsaki lab members for sharing the experimental data. This work was partially supported by the US National Science Foundation (NSF) grant CBET-1835000 (Z.C.), NIH grants R01-NS100065 (Z.C.), R01-MH118928 (Z.C.), L.C. was supported by the China Scholar Council fellowship (CSC201806140122).

REFERENCES

Agarwal, G., Stevenson, I.H., Berenyi, A., Mizuseki, K., Buzsaki, G. and Sommer, F.T. (2014). Spatially distributed local fields in the hippocampus encode rat position. *Science* **344,** 626-630.

Allen, T.A., Salz, D.M., McKenzie, S. and Fortin, N.J. (2016). Nonspatial sequence coding in CA1 neurons. *J. Neurosci.* **36**, 1547-1563.

Bansal, A.K., Truccolo, W., Vargas-Irwin, C.E. and Donogue, J.P. (2012). Decoding 3D reach and grasp from hybrid signals in motor and premotor cortices: spikes, multiunit activity, and local field potentials. *J. Neurophysiol*. **107**, 1337-1355.

Berenyi, A. *et al*. (2014). Large-scale, high-density (up to 512 channels) recording of local circuits in behaving animals. *J. Neurophysiol*. **111**, 1132-1149.

Berry, M.W., Browne, M., Langville, A.N., Pauca, V.P. and Plemmons, R.J. (2007). Algorithms and applications for approximate nonnegative matrix factorization. *Computational Statistics and Data Analysis*, **52**, 155-173.

Bishop, C. (2006). *Pattern Recognition and Machine Learning*. Springer.

Brown, E.N. *et al.* (1998). A statistical paradigm for neural spike train decoding applied to position prediction from ensemble firing patterns of rat hippocampal place cells. *J. Neurosci.* **18**, 7411-7425.

Buzsaki, G., Anastassiou, C.A. and Koch, C. (2012). The origin of extracellular fields and currents---EEG, ECoG, LFP and spikes. *Nat. Rev. Neurosci*. **13**, 407-420.

Buzsaki, G. (2015). Hippocampal sharp wave-ripples: a cognitive biomarker for episodic memory and planning. *Hippocampus* **25**, 1073-1188.

Buzsaki, G. and Tingley, D. (2018). Space and time: the hippocampus as a sequence generator. *Trends Cog. Sci.* **22**, 853-868.

Chang, E. (2015). Towards large-scale human-based mesoscale neurotechnologies. *Neuron* **86,** 68-78.

Chaudhuri, R., Gercek, B., Pandey, B., Peyrache, A. and Fiete, I. (2019). The intrinsic attractor manifold and population dynamics of a canonical cognitive circuit across waking and sleep. *Nat. Neurosci*. **22**, 1512-1520.

Chen, Z., Gomperts, S.N., Yamamoto, J. and Wilson, M.A. (2014). Neural representation of spatial topology in the rodent hippocampus. *Neural Computat*. **26**, 1-39.

Chen, Z., Grosmark, A.D., Penagos, H. and Wilson, M.A. (2016). Uncovering representations of sleep-associated hippocampal ensemble spike activity. *Sci. Rep.* **6**, 32193.

Chen, Z. and Wilson M.A. (2017). Deciphering neural codes of memory during sleep. *Trends. Neurosci*. **40**, 260-275.

Chung, J. E. *et al.* (2019). High-density, long-lasting, and multi-region electrophysiological recordings using polymer electrode arrays. *Neuron* **101**, 21-31.

Cichocki, A., Zdunek, R., Phan, A.H. and Amari, S-I. (2009). *Nonnegative Matrix and Tensor Factorizations: Applications to Exploratory Multi-Way Data Analysis and Blind Source Separation*. Wiley.

Ciliberti, D., Michon, F. and Kloosterman, F. (2018). Real-time classification of experience-related ensemble spiking patterns for closed-loop applications. *eLife* **7,** e36275.

Cunningham, J.P. and Yu, B.M. (2014). Dimensionality reduction for large-scale neural recordings. *Nat. Neurosci*. **17**, 1500-1509.

Davidson, T.J., Kloosterman, F. and Wilson, M.A. (2009). Hippocampal replay of extended experience. *Neuron*, **63**, 497-507.

Deng, X., Liu, D.F., Kay, K., Frank, L.M. and Eden, U.T. (2015). Clusterless decoding of position from multiunit activity using a Marked point process filter. *Neural Computat*. **27**, 1438-1460.

Drugowtisch, J. (2017). Variational Bayesian inference for linear and logistic regression. https://arxiv.org/pdf/1310.5438.pdf.

Ferbinteanu, J. and Shapiro, M.L. (2003). Prospective and retrospective memory coding in the hippocampus. *Neuron* **40**, 1227-1239.

Fernandez-Ruiz, A., Oliva, A., de Oliveira, E.F., Rocha-Almeida, F., Tingley, D. and Buzsaki, G. (2019). Long-duration hippocampal sharp wave ripples improve memory. *Science* **364,** 1082-1086.

Foster, D.J. (2017). Replay comes of age. *Ann. Rev. Neurosci*. **40**, 581-602.

Foster, D.J. and Wilson, M.A. (2007). Hippocampal theta sequences. *Hippocampus* **17**, 1093-1099.

Frank, L.M., Brown, E.N. and Wilson, M.A. (2000). Trajectory encoding in the hippocampus and entorhinal cortex. *Neuron* **27**, 169-178.

Frank, L.M., Stanley, G.B. and Brown, E.N. (2004). Hippocampal plasticity across multiple days of exposure to novel environments. *J. Neurosci*. **24,** 7681-7689.

Grosmark, A.D. and Buzsaki, G. (2016). Diversity in neural firing dynamics supports both rigid and learned hippocampal sequences. *Science* **351,** 1440-1443.

Gupta, A.S., van der Meer, M.A.A., D.S. Touretzky, D.S. and Redish, A.D. (2012). Segmentation of spatial experiences by hippocampal theta sequences. *Nat. Neuroci.* **15**, 1032-1039.

Hafting, T., Fyhn, M., Molden, S., Moser, M.-B., and Moser, E-I. (2005). Microstructure of a spatial map in the entorhinal cortex. *Nature* **436***,* 801-806.

Haggerty, D.C. and Ji, D. (2015). Activities of visual cortical and hippocampal neurons co-fluctuate in freely moving rats during spatial behavior. eLife *4,* e08902.

Honey, C.J., Sporns, O., Crmmoun, L., Gigandet, X., Thiran, J.P., Meduli, R. and Hagmann, P. (2009). Predicting human resting-state functional connectivity from structural connectivity. *Proc. Natl. Acad. Sci. USA* **106**, 2035-2040.

Hu, S., Ciliberti, D., Grosmark, A.D., Michon, F., Ji, D., Penagos, H., Buzsaki, G., Wilson, M.A., Kloosterman, F. and Chen, Z. (2018). Real-time readout of large-scale unsorted neural ensemble place codes. *Cell Rep*. **25**, 2635-2642.

Huang, Q., Jia, J., Han, Q. and Luo, H. (2018). Fast-backward replay of sequentially memorized items in humans. *eLife* **7,** e35164.

Hyvarien, A., Karhunen, J. and Oja, E. (2001). *Independent Component Analysis*. Wiley.

Ji, D. and Wilson, M.A. (2018). Firing rate dynamics in the hippocampus induced by trajectory learning. *J. Neurosci*. **28**, 4679-4689.

Jun, J.J. *et al*. (2017). Fully integrated silicon probes for high-density recording of neural activity. *Nature* **551**, 232-236.

Khodagholy, D., Gelinas, J.N., Thesen, T., Doyle, W., Devinsky, O., Malliaras, G.G. and Buzsaki, G. (2015). NeuroGrid: recording action potentials from the surface of the brain. *Nat. Neurosci.* **18**, 310-315.

Kloosterman, F., Layton, S.P., Chen, Z. and Wilson, M.A. (2014). Bayesian decoding using unsorted spikes in the rat hippocampus. *J. Neurophysiol.* **111**, 217-227.

Kurth-Nelson, Z., Economides, M., Dolan, R.J. and Dayan, P. (2016). Fast sequences of non-spatial state representations in humans. *Neuron* **91**, 194-204.

Le, Q.V., Karpenko, A., Ngiam, J. and Ng, A.Y. (2011). ICA with reconstruction cost for efficient overcomplete feature learning. *Advances in Neural Information Processing Systems (NIPS),* vol. 24, pp. 1017-1025. MIT Press.

Lee, D.D. and Seung, H.S. (1999). Learning the parts of objects by non-negative matrix factorization. *Nature* **401,** 788-791.

Linderman, S., Johnson, M.J., Wilson, M.A. and Chen, Z. (2016). A Bayesian nonparametric approach for uncovering rat hippocampal population codes during spatial navigation. *J. Neurosci. Methods* **263**, 36-47.

Liu, S., Grosmark, A.D. and Chen, Z. (2018). Methods for assessment of memory reactivation. *Neural Computat*. **30**, 2175-2209.

Liu, Y., Dolan, R.J., Kurth-Nelson, Z. and Behrens, T.E.J. (2019). Human replay spontaneously reorganizes experience. *Cell* **178**, 640-652.

Long, X. and Zhang, S-J. (2019). A novel somatosensory spatial navigation system outside the hippocampal information. https://www.biorxiv.org/content/10.1101/473090v1

Louie, K. and Wilson, M.A. (2001). Temporally structured replay of awake hippocampal ensemble activity during rapid eye movement sleep. *Neuron* **29**, 145-156.

Lubenov, E.V. and Siapas, A.G. (2009). Hippocampal theta oscillations are travelling waves. *Nature* **459**, 534-539.

Maboudi, K., Ackermann, E., de Jong, L.W., Pfeiffer, B.E., Foster, D., Diba, K. and Kemere, C. (2018). Uncovering temporal structure in hippocampal output patterns. *eLife* **7**, e34467.

Mao, D., Kandler, S., McNaughton, B.L., and Bonin, V. (2017). Sparse orthogonal population representation of spatial context in the retrosplenial cortex. *Nat. Commu*. **8***,* 243.

Olfsdottir, H.F., Bush, D. and Barry, C. (2018). The role of hippocampal replay in memory and planning. *Curr. Biol.* **28**, R37-R50.

Pastakova, E., Itskov, V., Amarasingham, A. and Buzsaki, G. (2008). Internally generated cell assembly sequences in the rat hippocampus. *Science* **321**, 1322-1327.

Patel, J., Fujisawa, S., Berenyi, A., Royer, S. and Buzsaki, G. (2012). Traveling theta waves along the entire septotemporal axis of the hippocampus. *Neuron* **75**, 410-417.

Patel, J., Schomburg, E.W., Berenyi, A., Fujisawa, S. and Buzsaki, G. (2013). Local generation and propagation of ripples along the septotemporal axis of the hippocampus. *J. Neurosci.* **33**, 17029-17041.

Pfeiffer, B.E. and Foster, D.J. (2013). Hippocampal place-cell sequences depict future paths to remembered goals. *Nature* **497**, 74-79.

Rey, H.G., Pedreira, C. and Quiroga, R.Q. (2015). Past, present and future of spike sorting techniques. *Brain Res. Bull*. **119**, 106-117.

Rossant, C. *et al.* (2016). Spike sorting for large, dense electrode arrays. *Nat. Neurosci*. **19**, 634-641.

Roumis, D.K. and Frank, L.M. (2015). Hippocampal sharp-wave ripples in waking and sleeping states. *Curr. Opin. Neurobiol.* **35,** 6-12.

Schmidt, B., Duin, A.A. and Redish, A. (2019). Disrupting the medial prefrontal cortex alters hippocampal sequences during deliberative decision making. *J. Neurophysiol*. **121**, 1981-2000.

Smith, E., Kellis, S., House, P. and Greger, B. (2013). Decoding stimulus identity from multi-unit activity and local field potentials alone the ventral auditory stream in the awake primate: implications for cortical neural prostheses. *J. Neural Eng*. **10**, 016010.

Stark, E. and Abeles, M. (2007). Predicting movement from multiunit activity. *J. Neurosci*. **27**, 8387-8394.

Singer, A., Carr, M.F., Karlsson, M.P. and Frank, L.M. (2013). Hippocampal SWR activity predicts correct decisions during the initial learning of an alternation task. *Neuron* **77**, 1163-1173.

Taxidis, J., Anastassioiu, C.A., Diba, K. and Koch, C. (2015). Local field potentials encode place cells ensemble activation during hippocampal sharp wave ripples. *Neuron* **87**, 590-604.

Townsend, R.G. and Gong, P. (2018). Detection and analysis of spatiotemporal patterns in brain activity. *PLoS Comput. Biol*. **14**, e1006643.

van der Maaten, L.J.P. and Hinton, G.E. (2008). Visualizing high-dimensional data using t-SNE. *Journal of Machine Learning Research,* **9**, 2579-2605.

Villette, V., Malvache, A., Tressard, T., Dupuy, N. and Cossart, R. (2015). Internally recurring hippocampal sequences as a population template of spatiotemporal information. *Neuron* **88**, 357-366.

Waldert, S., Lemon, R.N. and Kraskov, A. (2013). Influence of spiking activity on cortical local field potentials. *J. Physiol.* **591**, 5291-5303.

Wang, Y., Romani, S., Lustig, B., Leonardo, A. and Pastakov, E. (2015). Theta sequences are essential for internally generated hippocampal firing fields. *Nat. Neurosci.* **18**, 282-288.

Whitlock, J.R., Sutherland, R. J., Witter, M. P., Moser, M-B. and Moser, E-I. (2008). Navigating from hippocampus to parietal cortex. *Proc. Nat. Acad. Sci. USA* **105***,*14755-14762.

Wikenheiser, A.M. and Redish, A.D. (2015). Hippocampal theta sequences reflect current goals. *Nat. Neuroci.* **18**, 289-294.

Wu, W., Nagarajan, S. and Chen, Z. (2016). Bayesian machine learning: EEG/MEG signal processing measurements. *IEEE Signal Processing Magazine*, **33,** 14-36.

Zanos, T.P., Mineault, P.J. and Pack, C.C. (2011). Removal of spurious correlations between spikes and local field potentials. *J. Neurophysiol*. **105**, 474-486.

Zhang, H. and Jacobs, J. (2015). Traveling theta waves in the human hippocampus. *J. Neurosci.* **35**, 12477-12487.

Zhang, K., Ginzburg, I., McNaughton, B.L. and Sejnowski, T.J. (1988). Interpreting neuronal population activity by reconstruction: unified framework with application to hippocampal place cells. *J. Neurophysiol.* **79**, 1017-1044.

STAR METHODS

KEY RESOURCES TABLE

REAGENT or RESOURCE	SOURCE	IDENTIFIER
Deposited Data		
Datasets 1, 2	https://crcns.org/data-sets/hc/hc-11	N/A
Datasets 3, 4	http://buzsakilab.com/wp/datasets/.	N/A
Dataset 5	https://crcns.org/data-sets/hc/hc-3	N/A
Experimental Models: Organisms/Strains		
Long-Evans rats	Charles River Labs	RRID: RGD_2308852
Mice C57BL/6J	The Jackson Laboratory	stock no.: 000664
Software and Algorithms		
MATLAB	MathWorks	N/A
PYTHON	Open source	N/A
Custom code for various decoding methods	This paper	N/A

CONTACT FOR REAGENT AND RESOURCE SHARING

Further information and requests for resources should be directed to and will be fulfilled by the Lead Contacts, Zhe S. Chen (zhe.chen@nyulangone.org).

EXPERMIMENTAL MODEL AND SUBJECT DETAILS

All experimental studies were performed in accordance with the National Institutes of Health (NIH) *Guide for the Care and Use of Laboratory Animals* to ensure minimal animal use and discomfort, and were approved by the New York University School of Medicine (NYUSOM) Institutional Animal Care and Use Committee (IACUC). Long-Evans rats (n=3) and mice (n=2) were used in the behavior tasks, and were maintained on a 12:12-h light-dark cycle and housed individually with access to food and water.

METHOD DETAILS

Electrophysiological Recordings

Datasets 1 and 2: Circular track and linear track (rat 1). Male Long-Evans rats were bilaterally implanted with two 6-shank silicon probes (128 channels in total) parallel to the septo-temporal axis of the dorsal hippocampus. The silicon probe is a custom Buzsaki64SPL probe (NeuroNexus). This 6-shank silicon probe had 10 sites at each shank, and there were 4 extra channels spaced every 1.25 mm starting 1.25 mm from the tip of Shank 4 (6×10+4=64 channels). All sites were vertically staggered along the shank with 20 μm spacing between sites (**Figure S1C**). We selected one rat ('Achilles') in the analysis. The recording session consisted of a long (~4 hr) pre-RUN sleep epoch in a familiar room, followed by a RUN epoch (~45

minutes) in a novel circular maze (1 m diameter, Dataset 1) or a linear track (1.6 m long, Dataset 2). After the RUN epoch the animal was transferred back to its home cage in the familiar room where another long (~4 hour) post-RUN sleep was recorded. Details of experimental protocols and data have been published (Grosmark and Buzsaki, 2016; Chen et al., 2016). The electrophysiological data are publicly available (https://crcns.org/data-sets/hc/hc-11/).

Datasets 3 and 4: *T-maze and linear track (rat 2).* Two 256-channel (512 channels in total) custom-made silicon electrodes were implanted to the right hippocampus of the rat. The silicon probe is a custom Buzsaki256 probe with 32×8 array layout (**Figure S1C**). The two probes were perpendicularly aligned to each other in order to record along both the septotemporal and suiculo-fimbrial axis of the hippocampus. In the T-maze, rat was trained to perform a delayed alteration task, in which the animal had to choose either the left or the right arm at the decision point. After returning to the start area, the rat was confined for 10 seconds. In the next following trial, the rat had to choose the opposite direction and would obtain water reward with a correct choice. In the linear track, animal simply foraged back and forth to collect water reward. Details of experimental protocols have been published (Berenyi et al., 2014), and data are available at http://buzsakilab.com/wp/datasets/.

Dataset 5: Open field (rat 3). Male Long-Evans rats foraged and chased randomly dispersed drops of water or food on an elevated square platform (120 ×120 cm^2). The silicon probe consists of two 32-channel (4×8) array (**Figure S1C**). The probe was implanted in the rat's left and right dorsal hippocampi. Data are available at https://crcns.org/data-sets/hc/hc-3

Dataset 6: Circular T-maze (mouse 1 and mouse 2). Male mice were trained to perform a spatial alternating memory task in a circular T-maze. The silicon probe consists of a 64-channel (4×16) poly2 layout (**Figure S1C**). Each animal's recordings consisted of multiple sessions during 4-6 consecutive days, and each session lasted 50-60 min run epochs. At each session, animal was able to run 120-160 trials, with a minimum of 120 correct trials. The probe position was kept intact across sessions in order to assure the stability of LFP channels. Spikes were sorted separately for each session, yielding varying number of unit yields (**Table S1**).

Data Preprocessing and Analysis

Spike sorting. Extracellular representations of action potentials were extracted from recorded broadband (0.3 Hz-10 kHz) signals followed by threshold-based spike detection algorithm. We applied principal component analysis (PCA) to the spike waveform representations on the contact sites of a given shank, and the individual spikes were automatically clustered into groups with the lowest internal variance using the KlustaKwik algorithm (http://klustakwik.sourceforge.net/). For high-density probes, spikes were sorted using the Kilosort algorithm (https://github.com/MouseLand/Kilosort2) (Rossant et al., 2016). The clusters were manually refined by discarding multiunit clusters showing lack of clear refractories in the autocorrelogram, and groups with unstable firing patterns over time.

Bandpass filtering and calculation of instantaneous LFP amplitude. Broadband LFP signals were downsampled and filtered separately into different frequency bands. To extract theta-modulated LFP features, LFP signals were zero-phase filtered using a complex Morlet wavelet. We applied Hilbert transform (MATLAB function '**hilbert.m**') to the bandpass filtered LFP signals (e.g., theta band, gamma band, ripple band or >300 Hz) and obtained an analytic signal. We then computed the amplitude of the analytic signal to derive the instantaneous LFP amplitude at the specific frequency band.

Theta-band LFP demodulation. We applied a complex Morlet wavelet (with central frequency at 8 Hz) to the broadband LFP signal followed by (noncausal) zero-phase filtering. From the theta-band LFP, we applied demodulation using the following equation to obtain theta-demodulated LFP signals $y_d(t)$

$$y_d(t) = y(t)\exp\left(-\varphi(t)i\right)$$

where $i = \sqrt{-1}$, $y(t)$ denotes the band-pass filtered signals at the theta band, $\varphi(t)$ denotes the phase of the first principal component (PC) of the complex-valued, filtered multi-channel LFP signal within the theta frequency band. The first PC reflects the oscillatory component common to all channels. Demodulation preserves amplitude and relative timing of the wave at each channel, while discarding the theta-band oscillatory component (Agarwal et al. 2014).

Spike removal from raw LFPs. To remove putative spikes from the broadband LFP signal (up to 10 kHz), we ran the Kilosort algorithm (Rossant et al., 2016) to identify putative spikes across all channels. Once the spikes were identified in each channel, we removed the spikes, by using a linear interpolation from the start to end points of spike waveform or using a Bayesian spike removal algorithm (Zanos et al., 2011), and further obtained the resulting spike-free signal (**Figure 1F**). After high-pass filtering (>300 Hz), the filtered LFP signal $\mathbf{Y}_{\mathrm{LFP}}$ was decomposed into an additive sum of two components (**Figure 1G**):

$$\mathbf{Y}_{\mathrm{LFP}} = \mathbf{Y}_{\mathrm{spike-only}} + \mathbf{Y}_{\mathrm{spike-free}}$$

where $\mathbf{Y}_{\mathrm{spike-only}}$ denotes the spike-only component and $\mathbf{Y}_{\mathrm{spike-free}}$ denotes the spike-free component. The instantaneous amplitude of $\mathbf{Y}_{\mathrm{LFP}}$ (>300 Hz) was referred to as MUA.

Multichannel LFP Feature Extraction

Nonnegative matrix factorization (NMF). Let **Y** denote the *N*-by-*T* matrix consisting of nonnegative *N*-channel LFP amplitude features at a specific frequency band. NMF is aimed at finding an approximate low-rank matrix factorization form:

$$\mathbf{Y} \approx \mathbf{WH},$$

where **W** is a low-rank (*m*-by-*N, m*<*N*) nonnegative matrix, and **H** is an *m*-by-*T* nonnegative matrix. We interpreted the column vectors of **W** as a set of basis functions that reflected the spatially localized feature

in the latent space. There were many versions of NMF algorithms (Lee and Seung, 1999; Berry et al., 2007; Cichocki et al. 2009). We used the MATLAB function '**nnmf.m**' in our data analysis. Other NMF optimization algorithms (e.g., https://github.com/hiroyuki-kasai/NMFLibrary) also yielded similar results. We varied the model order *m* and compared the visualization effects. In the testing phase, given unseen data $\mathbf{Y}_{\text{test}}$, we fixed the basis function **W**, and estimated the $\mathbf{H}_{\text{test}}$ (with nonnegative elements) via the equation: $\mathbf{Y}_{\text{test}} \approx \mathbf{W}\mathbf{H}_{\text{test}}$.

Independent component analysis (ICA). Let **Y** denote the *N*-by-*T* matrix consisting of real or complex-valued *N*-channel LFP features at a specific frequency band. The ICA assumes that **Y** is a linear combination of independent source signals: **Y=MZ**, where **M** is a square mixing matrix, and **Z** denotes the *N*-by-*T* source signal matrix consisting of mutually statistically independent source signals. The source signals are assumed to non-Gaussian and sparsely represented. ICA is aimed to seek an optimal demixing matrix, **W**, operated on the **Y**, such that $\hat{\mathbf{Z}} = \mathbf{W}\mathbf{Y}$ recovers the independent source signals $\hat{\mathbf{Z}} \approx \mathbf{Z}$**,** subject to the scale and permutation ambiguity (Hyvarien et al. 2001). Provided that data **Y** are pre-whitened, ICA solves the following optimization problem

$$\min_{\mathbf{W}} \|\mathbf{W}\boldsymbol{y}\|_1 \qquad \text{s.t.} \quad \mathbf{W}\mathbf{W}^T = \mathbf{I}$$

where $\boldsymbol{y}$ is a column vector of **Y**.

For real-valued MUA features, we employed a reconstruction ICA (RICA) algorithm (Le et al., 2011). In contrast to ICA, RICA replaces the orthonormal constraint with a soft reconstruction penalty and allows an overcomplete representation (i.e., **W** is a non-square matrix). Mathematically, RICA solves the following penalized optimization problem

$$\min_{\mathbf{W}} \quad \|\mathbf{W}\boldsymbol{y}\|_1 + \rho\|\mathbf{W}^T\mathbf{W}\boldsymbol{y} - \boldsymbol{y}\|_2^2$$

where $\rho > 0$ is a regularization parameter. When $\mathbf{W}^T\mathbf{W} = \mathbf{I}$, it recovers the ICA as a special case. We used the MATLAB function '**rica.m**' in our data analysis.

Characterization of LFP traveling waves. To characterize the traveling wave patterns of multichannel LFP signals, we used the optical flow (vector field) method. Optical flow is commonly referred to the pattern of apparent motion of objects, and edges in a visual scene. In computer vision, the optical flow methods try to calculate the motion between two image frames which are taken at times *t* and $t + \Delta t$ at every voxel or pixel position. These methods are called differential since they are based on local Taylor series approximations of the frame images; that is, they use partial derivatives with respect to the spatial and temporal coordinates. For a 2D+*t* dimensional case, a voxel at location (x, y, t) with intensity $I(x, y, t)$ will have moved by $\{\Delta x\ ,\ \Delta y\ ,\ \Delta t\}$ between the two image frames, and the following *brightness constancy constraint* can be given:

$$I(x, y, t) = I(x + \Delta x, y + \Delta y, t + \Delta t)$$

Based on first-order Taylor series expansion, we derived

$$\frac{\partial I}{\partial x}\Delta x + \frac{\partial I}{\partial y}\Delta x + \frac{\partial I}{\partial t}\Delta t = 0 \quad \text{or} \quad \frac{\partial I}{\partial x}V_x + \frac{\partial I}{\partial y}V_x + \frac{\partial I}{\partial t} = 0$$

where $V_x = \frac{\Delta x}{\Delta t}$ and $V_y = \frac{\Delta y}{\Delta t}$. In the vector form, the above equation is:

$$\nabla\vec{\mathbf{I}} \cdot \vec{\mathbf{V}} = \nabla I_x V_x + \nabla I_y V_y = -\nabla I_t.$$

From the filtered (4-12 Hz or >300 Hz) multichannel LFP signals, we projected their Z-scored values onto a 2D image according to the array size. We then used the Horn-Schunck estimation method (MATLAB function '**opticalFlowHS**') to estimate the optical flow based on neighboring frames. The optical flow was represented and visualized by a 2D vector field (MATLAB function '**quiver.m**'), with arrows indicating the direction, and the size of arrow proportional to the scale. The spatiotemporal patterns of optical flow or vector field provided a characterization of the spatiotemporally local motion of traveling waves in space and time. For the purpose of decoding animal's position, we further temporally averaged the vector field movie at a frame rate of 10 Hz (i.e., bin size: 100 ms). These high-dimensional flow patterns were used in a simple linear decoding method (such as OLE). In real-time applications, estimation of optical flow can be implemented via graphic processing unit (GPU), such as NVIDIA optical flow SDK (https://developer.nvidia.com/opticalflow-sdk).

Stochastic neighbor embedding (SNE) of multichannel MUA features. The *t*-distributed SNE algorithm is a robust probabilistic dimensionality reduction method for visualization of high-dimensional data (van der Matten and Hinton, 2008). The goal of embedding was to approximate the probability distribution of high-dimensional MUA features when the same operation was performed on the low-dimensional (n=2 or 3) "image" of the MUA. We used the MATLAB function '**tsne.m**', with the default parameter setup ("Euclidean distance"). During animal's maze run, we color coded the embedded MUA features in a two-dimensional embedding space according to the animal's linearized position.

Decoding Analysis

Several spike-based or LFP-based decoding strategies were investigated (**Table S1** and **Figure S2C**). In all decoding analyses, spikes or LFP features were Z-scored across neurons or channels, respectively.

Likelihood-based spike decoding. From the sorted ensemble spikes, we constructed the place receptive fields for hippocampal pyramidal neurons ('place cells'). Let $\boldsymbol{\lambda}_c$ denote the place field of the c-th (c=1,…,C) neuron for the binned position; assuming Poisson probability firing for each neuron, the likelihood function given the observed sorted spike activity $\boldsymbol{y}_{1:T} = \{y_{c,t}\}_{C\times T}$ within a fixed-time interval is given as follows (Zhang et al., 1998; Davidson et al., 2009):

$$P(\boldsymbol{y}|\boldsymbol{x}) = \prod_{t=1}^{T}\prod_{c=1}^{C} \text{Poisson}(y_{c,t}|\boldsymbol{\lambda}_c(\boldsymbol{x}), \Delta)$$

where $\boldsymbol{\lambda}_c(\boldsymbol{x})$ denotes the place field or spatial tuning curve for the *c*-th neuron, and Δ denotes the temporal bin size. The likelihood was normalized between 0 and 1 (as probability) for all position bins. The maximum likelihood estimate (MLE) seeks to find the optimal estimate $\hat{\boldsymbol{x}}$ such that

$$\hat{\boldsymbol{x}}_{\text{m.l.e.}} = \text{argmax}_x P(\boldsymbol{y}|\boldsymbol{x})$$

To extend the likelihood-based decoding to Bayesian decoding, we incorporated a temporal Gaussian prior conditional on the previously decoded position (Brown et al., 1998; Agarwal et al. 2014).

LFP decoding based on optimal linear estimation (OLE). We used the standard OLE method previously described before (Agarwal et al. 2014). We assumed that the decoded variable $\boldsymbol{x}$ can be linearly reconstructed from neural activity $\boldsymbol{y} = \{y_c\}$ using a set of functions $\phi(\boldsymbol{x})$

$$\hat{\boldsymbol{x}} = \text{argmax}_x \sum_c y_c\, \phi_c(\boldsymbol{x})$$

We further assumed a local basis function $\phi_c(\boldsymbol{x})$ for the decoded position variable. In one-dimensional environment, we mapped the linearized position (with length *L*) via *K* equally spaced von Mises functions characterized by a circular variable $\theta = 2\pi x/L$: $B_k(\theta) = \exp\,(\kappa\cos(\theta - \theta_k))$ for *k*=1,…,*K*. The original linear representation can be reformulated as

$$\hat{\boldsymbol{\theta}} = \text{argmax}_{\boldsymbol{\theta}} \sum_c y_c \sum_k v_{c,k} B_k(\boldsymbol{\theta})$$

The optimization of parameter $\boldsymbol{V} = \{v_{c,k}\}$ will be solved by a least-squared (LS) solution

$$\hat{\boldsymbol{V}} = \text{argmin}_{\boldsymbol{V}} \sum_t \|\boldsymbol{y}_t - \boldsymbol{V}\boldsymbol{B}(\boldsymbol{\theta}_t)\|$$

where $\boldsymbol{y}_t$ denotes the vectors of spike count or multichannel LFP features at time *t*, and $\boldsymbol{B}(\boldsymbol{\theta}_t) = [B_1(\boldsymbol{\theta}_t), \ldots, B_K(\boldsymbol{\theta}_t)]$ denotes a *K*-dimensional vector that expands the position in the basis. Unless stated otherwise, we used *K*=75, $\kappa = 100$ and a temporal bin size of 100 ms (maze run) or 20 ms (ripple events). In all decoding methods, all LFP features were first averaged within each time bin and then Z-scored across all channels. We rescaled the OLE output between 0 and 1 via a softmax operation.

In addition, we considered incorporating the prior history of LFP activity (such as $\boldsymbol{Y}_{t-1}$) as additional covariance in the linear regression estimator. However, this was at the cost of doubling computational complexity and potential overfitting.

In the open field, we mapped the two-dimensional position by replacing *K* von Mises basis functions with a set of two-dimensional Gaussian tiling (Agarwal et al., 2014)

$$B_k(\boldsymbol{x}) = \frac{1}{2\pi\sqrt{|\boldsymbol{\Sigma}|}} \exp\left(-(\boldsymbol{x}-\boldsymbol{\mu}_k)^T \boldsymbol{\Sigma}^{-1} (\boldsymbol{x}-\boldsymbol{\mu}_k)\right)$$

Where the vectors $\boldsymbol{x}$ represents the animal's 2D position, and $\boldsymbol{\Sigma}$ denotes the (diagonal or isotropic) covariance, and $\{\boldsymbol{\mu}_k\}$ denotes the mean vectors of *K* Gaussians that tile the field. We used *K*=144 and temporal bin size of 300 ms for the open field environment.

LFP feature likelihood-based decoding. We designed a Gaussian likelihood-based decoder (i.e., noninformative prior) based on LFP features

$$y_c \sim \text{Gaussian}(\lambda_c, \sigma_c^2)$$

where σ_c^2 denotes the variance, and the mean λ_c is represented by a sum of one or two-dimensional basis functions

$$\lambda_c = \sum_k v_{c,k} B_k(\boldsymbol{x}) \quad \text{or} \quad \lambda_c = \sum_k v_{c,k} B_k(\boldsymbol{\theta})$$

The Gaussian log-likelihood function, denoted as $\mathcal{L}$, is written as

$$\mathcal{L} = \sum_{t=1}^{T} \sum_{c=1}^{C} \frac{1}{2} \ln(2\pi\sigma_c^2) - \frac{\left(\boldsymbol{y}_{c,t} - \lambda_{c,t}\right)^2}{2\sigma_c^2}$$

where $\lambda_{c,t} = \sum_k v_{c,k} B_k(\boldsymbol{x}_t)$. The unknown parameters $\{v_{c,k}, \sigma_c^2\}$ were estimated from the maximum likelihood estimation.

LFP feature selection used for decoding. For each channel, we extracted the instantaneous LFP amplitude and phase at specific frequency bands. We systematically investigated the LFP features at the following frequency bands: theta (4-12 Hz), slow gamma (30-80 Hz), fast gamma (80-140 Hz), ripple (140-250 Hz), and ultra-high frequency (>300 Hz).

LFP decoding by imposing a sparsity constraint. In the OLE method, the traditional linear least-squared (LS) regression method is subject to overfitting in the presence of high-dimensional features. To improve generalization and assist variable, we used a sparse Bayesian linear regression method based on variational Bayes (VB) and automatic relevance determination (ARD) (Bishop, 2016; Wu et al., 2016). The mathematical details and MATLAB implementation are referred to (Drugowitsch et al., 2017). We extended the multi-input single-output (MISO) regression problem to a multi-input multi-output (MIMO) regression problem. Finally, the VB inference produced the posterior mean and posterior variance of the individual parameter in $\boldsymbol{V} = \{v_{i,k}\}$. For the purpose of variable selection, the parameter with a small mean and a small variance would be discarded. See **Figure S10** for an illustration of encoding and decoding application.

Bayesian hidden Markov model (HMM) for unsupervised learning decoding analysis. To discover latent structures of large-scale hippocampal population codes, we developed a HMM for analyzing hippocampal ensemble spike activity during spatial navigation and sleep (Chen et al. 2014; Chen et al.,

2016; Linderman et al. 2016). In a basic HMM, we assumed that the latent state process follows a first-order discrete-state Markov chain $\{S_t\} \in \{1,2,\cdots,N_s\}$, and the observations of neural activity at discrete time index t, follow a conditional probability distribution (conditioned on the latent state S_t). In the case of nonnegative features (either in the form of neuronal spike counts or multisite MUA features), we assumed a Poisson probability associated with associated tuning curve functions $\boldsymbol{\Lambda} = \{\boldsymbol{\lambda}_c\} = \{\lambda_{c,i}\}$. The joint probability distribution of observed and latent variables are given by

$$P(\boldsymbol{y}_{1:T}, S_{1:T}|\boldsymbol{\pi}, \boldsymbol{P}, \boldsymbol{\Lambda}) = p(S_1|\boldsymbol{\pi}) \prod_{t=2}^{T} p(S_t|S_{t-1}, \boldsymbol{P}) \prod_{t=1}^{T} p(\boldsymbol{y}_t|S_t, \boldsymbol{\Lambda})$$

where $\boldsymbol{P} = \{P_{ij}\}$ denotes an N_s -by-N_s state transition matrix, with P_{ij} representing the transition probability from state i to j; $\boldsymbol{\pi} = \{\pi_i\}$ denotes a probability vector for the initial state S_1; $y_{c,t}$ denotes the number of spike counts from cell c within the t-th temporal bin (bin size: 100 ms during wake and 20 ms during ripples) and $\boldsymbol{y}_{1:T} = \{y_{c,t}\}_{C\times T}$ denotes the time series of C-dimensional neural response vector. In the case of spike counts, we assumed the conditional probability distribution has a factorial form: $p(\boldsymbol{y}_t|S_t, \boldsymbol{\Lambda}) = \prod_{c=1}^{C} Poisson(y_{c,t}|\lambda_{c,S_t})$, which defined the products of conditionally independent Poisson distributions. We developed a Bayesian inference procedure to identify the unknown parameters $\{\boldsymbol{\pi}, \boldsymbol{P}, \boldsymbol{\Lambda}\}$ and the latent state sequences $\{S_{1:T}\}$ (Chen et al., 2014). We further developed a Bayesian nonparametric version of the HMM, the hierarchical Dirichlet process-HMM (HDP-HMM), which extends the finite-state HMM with a nonparametric HDP prior, and inherits a great flexibility for modeling complex data (Linderman et al., 2016). The associated Markov chain Monte Carlo (MCMC)-based inference algorithm allowed us to infer the optimal model order N_s.

LFP feature resampling. In the HDP-HMM, the assumed observations were Poisson-distributed spike counts (nonnegative integers). Therefore, we need to adapt the likelihood model of the HMM to accommodate LFP-feature observations. In the case of nonnegative LFP features $\boldsymbol{y}_t$ (e.g., derived from NMF operated on nonnegative MUA or LFP_θ power), we generated the same size of random samples from a desired Poisson distribution based on a rank-invariant resampling procedure (Honey et al., 2009), and replaced the original samples with the ordered new samples (by keeping their rank or order unchanged). We treated $\tilde{\boldsymbol{y}}_t$ as the pseudo spike count observations and then repeated the same Bayesian inference procedure assuming a new Poisson likelihood $p(\tilde{\boldsymbol{y}}_t|S_t, \boldsymbol{\Lambda}) = \prod_{j=1}^{N} Poisson(\tilde{y}_{j,t}|\lambda_{j,S_t})$. For the real-valued Z-scored LFP features, a similar resampling procedure was also employed. A schematic illustration of the resampling procedure is shown in **Figure S7**. The choice of the mean statistic (say 10) in the new Poisson distribution was ad hoc, yet the final performance was robust with respect to a wide range of the Poisson mean statistic.

Identification of ripples and awake and sleep replay candidate events. We first used the electromyography (EMG) and LFP for sleep staging. NREM sleep was primarily determined by the low EMG amplitude, high delta/theta power ratio, the presence of slow waves and sleep spindles in LFP activity. REM sleep was determined by the low EMG amplitude and high theta/delta power ratio. SPW-Rs were identified based on a previously described method (Grosmark and Buzsaki, 2016). The integrated power of the filtered LFP signal was calculated in a sliding window for each electrode. To identify the candidate

events of memory replay during immobility and NREM sleep (**Figure 2A**), we used a combined criterion of hippocampal LFP amplitude at ripple band (140-250 Hz) and total spike count (threshold >mean+3 SD). For visual inspection, we computed the spectrogram to assist identification. Time-frequency analysis was done using the established multitaper method (Chronux; http://chronux.org/). We selected subsets of candidate events during immobility (in the maze or sleep box) and post-NREM periods for MUA or clustered spike-based decoding analysis.

Prospective decoding and prediction of animal's future spatial decision-making. In goal-directed navigation tasks, we developed a look-ahead decoding strategy to predict animal's future decision (L vs. R turns) based on either ensemble spikes or LFP features collected in the central arm of T-maze. During the training phase, we correlated the animal's future position at the L/R arm with neural activity with a time lag (0.5-1.5 s, 100 ms temporal bin size) while animal ran in the central arm (see **Figure 5A** for schematic illustration). We assessed the "mode" of decoded L vs. R-turn trajectories and determined the prediction outcome based on their sums of weighted scores---the one with a higher cumulative sum was deemed the winner. The score at each time point was weighted with a slow decay from the future to the past. For instance, we used a linear decay vector [1, 0.9, 0.8, 0.7, 0.6], by imposing a larger weight on the future predicted outcome (yet the ultimate prediction outcome was insensitive to the exact values in the decay vector). To assess the prediction accuracy, we conducted 10-fold cross-validation. In addition, we ran 1,000 Monte Carlo runs (by randomly selecting 90% training trials in each run) and reported the mean±SD classification accuracy. As control for each strategy, we also performed 1,000 random shuffles and computed the chance-level accuracy.

Furthermore, we trained a linear support vector machine (SVM) classifier (Bishop, 2006) to predict animal's future decision based on the joint (MUA+LFP_θ) features. The SVM is a discriminative supervised learning model that constructs the classification boundary by a separating hyperplane with maximum margin. Specifically, the SVM maps the input **x** into high-dimensional feature spaces, which allows linear or nonlinear classification, as follows:

$$y_i = \sum_{i=1}^{N} K(\mathbf{x}, \mathbf{x}_i) + b$$

where y_i denotes the class label for the training sample $\mathbf{x}_i$, *b* denotes the bias, and $K(\mathbf{x}, \mathbf{x}_i)$ denotes the kernel function. For the ease of interpretation, we used a linear kernel in the SVM (MATLAB Machine Learning Toolbox '**fitcsvm**' function). In addition to the classification accuracy, we also reported the AUROC (area under ROC curve) statistic. An AUROC value of 0.5 indicates a chance level, whereas a high AUROC value (close to 1) implies excellent performance.

Real-Time Decoding

Real-time MUA decoding based on the OLE method. Our real-time MUA decoding operation consisted of three steps. *Step 1*: Broadband voltage signals were filtered (>300 Hz) in data acquisition hardware. In

real-time processing, we used a causal, low-latency 5th-order Butterworth finite-impulse response (FIR) filter. *Step 2*: In the memory buffer (20 ms during ripples and 100 ms during run), multichannel LFP signals were processed by a Hilbert transform in parallel (using multi-core CPU), and instantaneous LFP amplitude features were computed. The memory was constantly updated in time. *Step 3:* Position was reconstructed based on a pretrained linear map ***V***. The pipeline was initially implemented in MATLAB R2019 (MathWorks), and optimized by C/C++ implementation (with Intel complier). We tested all real-time operations on a desktop (3.6 GHz 4-core Intel® i7700 CPU, with Windows®10 OS, Visual Studio 2017 and Intel® Parallel Studio XE 2018 environment).

Once the LFP features were computed across channels and averaged within each time bin, the remaining computational complexity of OLE operation was $O(N*L)$ per time bin (where N denotes the number of channels and L denotes the number of spatial bins), which was split into multiple threads in parallel for computational speedup. Since the computational bottleneck was the Hilbert transform. Further speedup in the computation of FIR filtering and Hilbert transform may be done by hardware implementation, such as FPGA (Field Programmable Gate Array).

Real-time significance assessment of decoded memory replay. An important step in analyzing online hippocampal memory replay is to assess the statistical significance of decoded spatial trajectory (Hu et al., 2018). To assess the significance of the MUA decoding result, we ran shuffle analyses. To accommodate the real-time computation, we performed and saved two types of pseudorandom shuffles (i.e., channel order shuffle by permutating columns and receptive field shuffle by circular-shifting each column) in advance and directly applied those in online decoding.

We used Hilbert transform to computed the LFP amplitude at ripple band (140-250 Hz) for a preselected channel that shows the largest ripple amplitude, and then compared ripple band amplitude with a predetermined threshold (e.g., mean+SD) to detect the onset of candidate event (**Figure 6D**). Since the decoding speed is ultrafast, we used a "decode-as-you-go" strategy. Specifically, we calculated >300 Hz high-passed amplitudes features (MUA) for all recording channels and continuously decoded the content for each time bin. But the significance assessment of the candidate event was only ran after the length of event above 3 bins. Once the significance assessment is started, we ran 2,000 (1,000 for each type of shuffle operation) random shuffle decoding analysis for the whole event at each time step and computed the Monte Carlo *P*-value (based on the distance correlation measurement). After the P-value is calculated, we update the cumulative score as follows

$$Score_i = \begin{cases} Score_{i-1}, & \text{if Ripple_band amplitude} < \text{threshold or } P_{value}(i) > 0.05 \\ Score_{i-1} - \log\left(P_{value(i)}\right), & \text{otherwise} \end{cases}$$

where *i* denotes the time bin index, and $Score_0 = 0$ at the time of event onset. Once the online cumulative score was above a predetermined threshold (e.g., $-3\log(0.01)$ used in our current analyses), the event was deemed statistically significant and we reset the cumulative score to be 0. All analyses were first implemented in MATLAB scripts and then optimized in C/C++ code.

QUANTIFICATION AND STATISTICAL ANALYSIS

Statistical assessment of decoding. During maze run (velocity threshold: 5-15 cm/s depending on the spatial environment), we evaluated the decoding accuracy by the absolute error between the animal's actual position and the decoded position: $|\boldsymbol{x}_{\text{true}} - \hat{\boldsymbol{x}}_{\text{decode}}|$ (where $\hat{\boldsymbol{x}}_{\text{decode}}$ was derived from a specific decoding strategy using either clustered spikes, MUA or LFP-based features). We used 10-fold cross-validation to assess the median decoding error, and computed the bootstrapped standard deviation (SD).

During ripple events, we computed the distance correlation (Liu et al., 2018), and then computed 2,000 random shuffles for each event to derive the Z-score statistic or Monte Carlo *P*-value. For spike-based likelihood decoding, we used cell identity shuffling and receptive field shuffling; for MUA decoding, we used channel order shuffling and linear map shuffling (with respect to the rows of matrix ***V*** from the OLE). Among different types of shuffling operations, we used the worst Z-score or Monte Carlo *P*-value as the final shuffle statistics.

Region-specific assessment of decoding. High-density silicon probes enabled us to record multiple regions (e.g., CA1, CA3, dental gyrus) or layers of the hippocampus. To assess the region-specific contribution to specific decoding strategy, we first split the channels according to their implanted anatomical regions (**Figure S3**). To control the imbalance of channel counts between regions, we randomly selected the matched number of channels from other regions and repeated the same decoding analysis. We repeated the random selection for 1,000 times and compared their Monte Carlo statistics.

DATA AND SOFTWARE AVAILABILITY

All data needed to evaluate the conclusions in the paper are present in the paper and/or the supplementary materials. Some datasets included in this study are publicly available at https://crcns.org/data-sets/hc/ or are available upon request. Custom MATLAB and Python scripts can be downloaded from www.cn3lab.org/software.html.

Figure 1. Spatial Distributed Hippocampal Recordings Encode Rat Position during Maze Running

(A) Illustration of processing raw voltage traces of hippocampal recordings into three different signals: clustered spikes (red), filtered LFP at theta band (blue), and high-pass filtered signal (>300 Hz, green).

(**B**) Comparison of rat's decoded movement trajectory on a circular track (Dataset 1) based on three different signals derived from (**A**): clustered spikes (red), demodulated LFP theta (referred to as LFP_θ, amplitude plus phase, blue), high-pass filtered (>300 Hz) LFP amplitude (referred to as MUA, green). The rat's position is marked by the black line. In all illustrations, we used an OLE method trained by sparse Bayesian regression.

(C) Histograms (left) and error cumulative distribution function (CDF; right) curves of 10-fold cross-validated decoding errors during maze run. Augmenting the covariate with their respective history at the decoded preceding time bin ('history decoding') further improved the cross-validated decoding accuracy in each case by ~10% (dotted line in the CDF curves; two-sample Kolmogorov-Smirnov test, $P=1.4\times10^{-4}$, 4.6×10^{-5}, 1.1×10^{-2} for three respective panels). The numbers in the CDF plot indicate the median position decoding error of two CDF curves.

(D) Illustration of position decoding in 2D open field environment (Dataset 5) based on the same decoding strategy derived from clustered spikes, LFP_θ, MUA, and joint LFP (LFP_θ+MUA) features. The animal's actual position is marked in black. We used a Bayesian filter decoder with a Gaussian temporal prior for all features. To reduce input correlation of multichannel LFP features, we conducted a PCA-whitening step before the encoding procedure. See also **Movie S1**.

(E) Comparison of decoding error CDF curve derived from the four different signals shown in (**D**). Numbers indicate the corresponding median position decoding error.

(F) Decomposition of a broadband raw voltage trace (*1st row*) into the sum of a spike-free component (*2nd row*) and a spike-only component (*3rd row*). To investigate the effect of spike waveform and amplitude, we normalized individual spike waveforms by their respective peak amplitudes and derived the signal in the 4th row. Color ticks in the top represent identified spikes from clustered units (with the associated averaged spike waveform).

(**G**) Down-sampled (1,250 Hz) and high-pass filtered (>300 Hz) version of the four signals in (**F**).

(H) Comparison of decoding error CDF curve derived from the four different signals shown in (**G**). Numbers indicate the corresponding median position decoding error.

Figure 2. Spatial Distributed Hippocampal LFP Patterns Encode Rat Position during Ripple Events
(**A**) Illustration of a broadband hippocampal recording trace (black) during a candidate replay event. The candidate event was determined by a joint criterion (Methods) using the total unclustered spike count (red) and ripple-band amplitude (blue). The red and blue horizontal dotted lines indicate their respective thresholds.

(B) Three representative example trajectories of virtual maze positions decoded from the spikes during hippocampal ripple periods, derived from a maximum likelihood estimator (MLE) using clustered spikes ("ground truth"; *top*), from an optimal linear estimator (OLE) with sparse Bayesian regression using clustered spikes (*middle*), and from an OLE with sparse Bayesian regression using MUA (*bottom*). Dark pixels show high probability values.

(C) Histogram comparisons between the three estimators shown in (**B**).

(D) Comparison of Z-scored statistics of distance correlation (see Methods) for ripple replay candidate events (n=727 ripples during waking and NREM sleep). Decoding methods (OLE or Bayesian) and features (MUA or clustered spikes) are labeled in each paired comparison. Dashed lines mark the Z-score value of 2.33 (P=0.01).

Figure 3. Unsupervised Learning Methods for Extracting Multichannel MUA Features

(A) Illustration of NMF (*top*) and RICA (*bottom*) methods for extracting lower-rank features from MUA during maze run (Dataset 1). After sorting, the position-average patterns (from the rows of NMF's matrix **H** or RICA's matrix **Z**) yielded localized position-tuned features covering the entire track (similar to "place fields").

(B) Same as (**A**), during ripple events. The virtual position was decoded from clustered spikes.

(C) A Bayesian HMM was used for inferring latent state sequences $\{S_1(t)\}$ and $\{S_2(t)\}$, based on the spike ensembles and MUA features, respectively. The sorted ensemble spikes are assumed to be Poisson distributed. The lower-rank MUA features were obtained from the NMF's matrix **H**, followed by a feature resampling procedure (Methods). The matrix frame color (green, blue, red) represent the source of feature matrix (spike count, **H, Z**).

(D) During maze running, the Bayesian HMM analysis revealed a strong one-to-one correspondence map between the animal's position and the inferred latent states $\{S_1(t), S_2(t)\}$, as well as between $\{S_1(t)\}$ and $\{S_2(t)\}$ (upon sorting). These consistency results indicated that the most valued signal in MUA is clustered spikes (*top row:* bases on NMF; *bottom row*: based on RICA). Label color (S_1 in green and S_2 in blue or red) represents the latent state sequence derived from clustered spikes and lower-rank features (**H** or **Z**).

(E) During ripples in the absence of behavior measures, the Bayesian HMM analysis also revealed a correspondence map between $\{S_1(t)\}$ and $\{S_2(t)\}$, which were derived from the ensemble spikes and MUA features (*top row:* bases on NMF; *bottom row*: based on RICA), respectively. Label color same as (**D**).

Figure 4. Spatiotemporal Patterns of Multisite Recorded Hippocampal LFP Encode Run Trajectories

(A) Illustration of optical flow estimation and visualization by 2D vector field. High-density silicon probe recordings (8 shank, 32 sites each rank) in the same hippocampus in the transversal (T) and longitudinal (L) axes of a rat are shown separately (Dataset 3). Each 2D vector was visualized as an arrow (characterized by size and direction). (i) Background color in the raw map represents the voltage of filtered LFP traces. (ii) Background was color coded according to the arrow direction.

(B) Optical flow estimated from band-pass filtered (4-12 Hz) 2×256-site recorded LFP signals show position-dependent patterns on a T-maze (Dataset 3). The vector field patterns showed trial-by-trial consistency. See **Movie S3** for the demonstration of clear propagating wave patterns.

(C) Schematic of extracting parallel and independent spatiotemporal features from hippocampal field potentials at theta (4-12 Hz) and ultra-high (>300 Hz) frequency bands. Features are labeled as ① ② ③ ④.

(D) Comparison of median position decoding error during maze run derived from four different spatiotemporal features in (**C**) and their feature combinations (Dataset 3). Error bar shows the bootstrapped SD.

Figure 5. LFP, MUA and Spike-based Features Predict Animal's Decision-making in the Mouse

(A) Schematic of prospective decoding, with time lag of 0.5-1.5 s (5-15 temporal bins, 100 ms bin size) prior to the choice point in the T maze.

(B) Comparison of cross-validated prediction accuracy between clustered spike-based and joint (LFP_θ+MUA) decoding strategies (Dataset 6). Mean and SD results were pooled over multiple sessions. *Left panel*: mouse 1 (n=4 sessions, n=120 correct trials per session); *right panel*: mouse 2 (n=4 sessions, n=120 correct trials per session).

(C) *Top panel:* SVM classification accuracy (for mouse 1). The peak classification rate from cross-validation was ~90% and the AUROC statistic was ~0.94. *Bottom panel*: Boxplot statistics of animal's actual location at specific temporal bins across all tested trials. The classification accuracy degraded with increased variability in the range of animal's location.

Figure 6. Robustness and Scalability of Different Decoding Strategies

(A) Cross-session decoding error matrices summarize within-session and between-session assessment of the LFP_θ and MUA decoding strategies in five consecutive run sessions (Dataset 6, Mouse 1). Combining two complementary features further improved the decoding accuracy. The number in the matrix shows the median position decoding error. Sessions (labeled by A,B,C,…E) were separated by ~24 hours.

(B) Average statistics of the *k*-th ($-4 \leq k \leq 4$) diagonal of cross-session decoding error matrices in (**A**). *k*=0 implies within-session decoding; *k*<0 (lower diagonal) implies training on historical sessions and testing the subsequent sessions in time; *k*>0 (upper diagonal) implies the reverse order.

(**C**) MUA decoding strategy (green: 20 ms; blue: 100 ms bin size) with respect to the number of channels, *N*. In the computer simulations, the linear mapping was assumed of dimensionality $N\times145$ for a 1D environment with 145 spatial bins. Horizontal green and blue dotted lines mark 20 ms and 100 ms, respectively. Signals were down-sampled (up to 1,250 Hz) and high-pass filtered (>300 Hz) prior to computation. Shaded areas correspond to the SD from 1,000 realizations.

(D) Illustration of online detection and assessment of rat hippocampal memory replay (Dataset 1). First, given the raw extracellular voltage trace (1st row), we identified the onset of candidate event using a threshold criterion based on the ripple band amplitude (2nd row). Next, we continuously decoded "spatial trajectory" from hippocampal MUA at each time bin (20 ms bin size; 3rd row). Once the duration of candidate event was more than 3 bins, the significance of decoded "spatial trajectory" was assessed using online shuffling statistics (4th row). The Monte Carlo *P* value was computed based on distance correlation (red). An accumulative score (blue) was computed as we continuously updated the assessment if *P*<0.05 (red horizontal dashed line). Finally, a significance decision for spatial memory replay was made when the accumulative score was above a threshold (blue horizontal dashed line). The accumulative score was set to 0 at the detection onset and reset to 0 when the cumulative score threshold was reached. The computation time for online evaluation at each temporal bin is shown in the last row.

Table 1. Comparison of four different hippocampal LFP spatiotemporal features (*N* denotes the channel count) and their potential decoding applications.

LFP features	# dim.	Operation	Spatiotemporal characteristic	Decoding applications
demodulated theta (4-12 Hz)	2*N*	bandpass filtering, Hilbert transform, PCA	spatially global	run, REM sleep
theta flow (4-12 Hz)	2*N*	bandpass filtering, optical flow estimation	spatially local, temporally local	run, REM sleep
>300 Hz amplitude	*N*	high-pass filtering, Hilbert transform	temporally independent	run, ripple sequences, theta sequences
>300 Hz flow	2*N*	high-pass filtering, optical flow estimation	spatially local, temporally local	run, ripple sequences, theta sequences

Figure 1

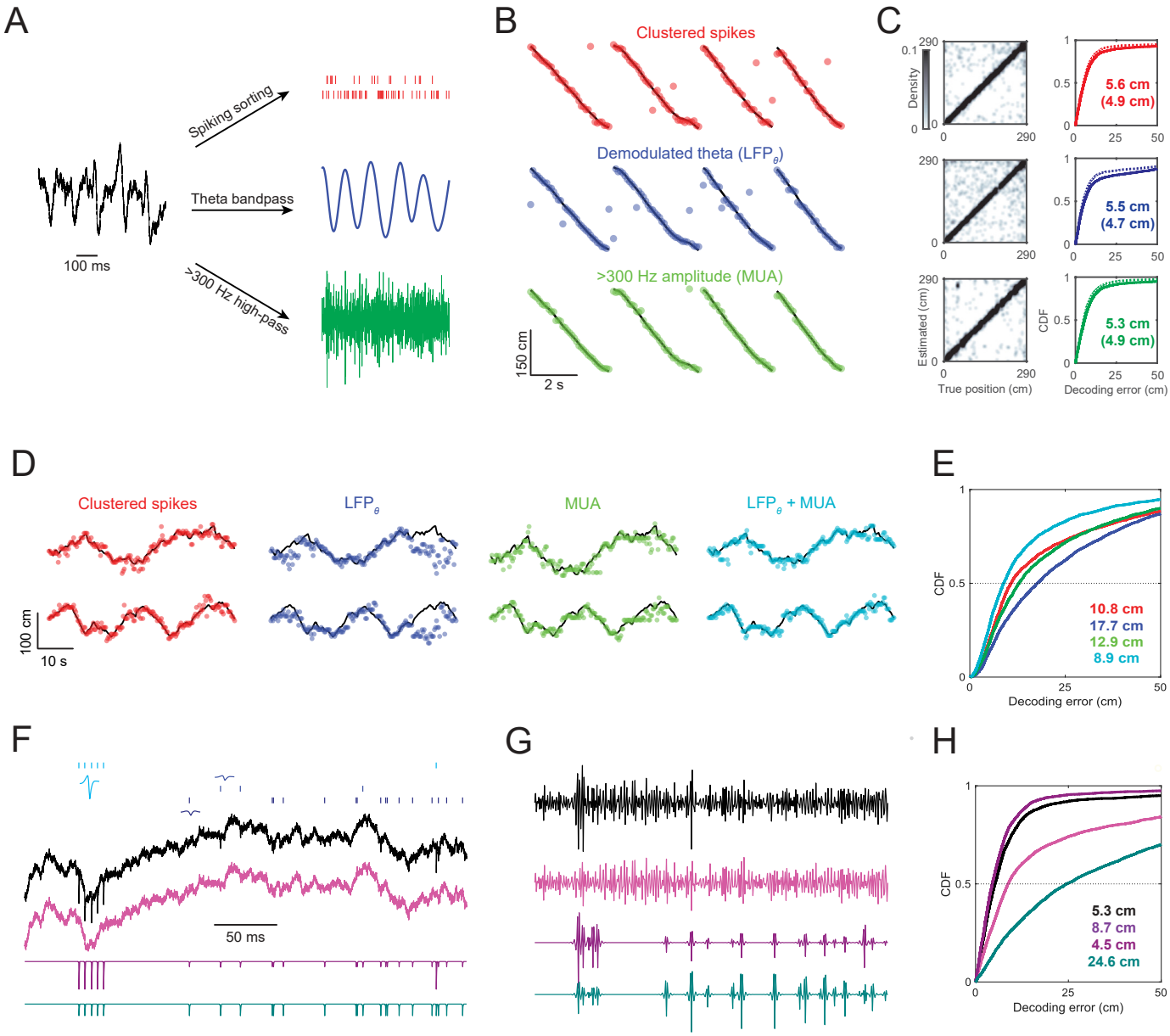
A
Spiking sorting
Theta bandpass
>300 Hz high-pass
100 ms
B
Clustered spikes
Demodulated theta (LFP$_\theta$)
>300 Hz amplitude (MUA)
150 cm
2 s
C
Density
Estimated (cm)
True position (cm)
CDF
Decoding error (cm)
5.6 cm
(4.9 cm)
5.5 cm
(4.7 cm)
5.3 cm
(4.9 cm)
D
Clustered spikes
LFP$_\theta$
MUA
LFP$_\theta$ + MUA
100 cm
10 s
E
CDF
Decoding error (cm)
10.8 cm
17.7 cm
12.9 cm
8.9 cm
F
50 ms
G
H
CDF
Decoding error (cm)
5.3 cm
8.7 cm
4.5 cm
24.6 cm

Figure 2

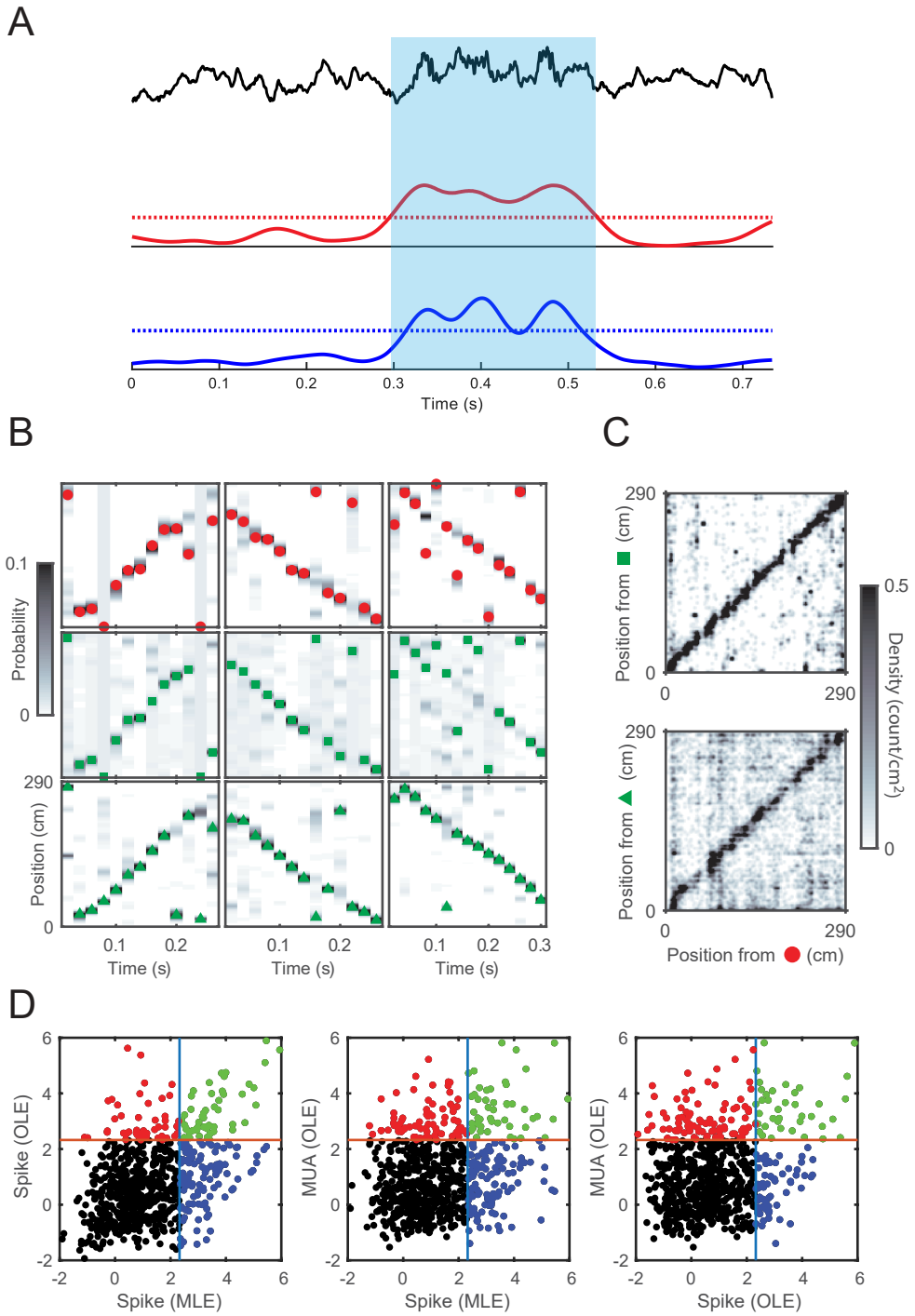
A
0
0.1
0.2
0.3
0.4
0.5
0.6
0.7
Time (s)
B
0.1
Probability
0
290
Position (cm)
0
0.1
0.2
Time (s)
0.1
0.2
Time (s)
0.1
0.2
0.3
Time (s)
C
290
Position from (cm)
0
0
290
290
Position from (cm)
0
0
290
Position from (cm)
0.5
Density (count/cm²)
0
D
6
4
2
0
-2
Spike (OLE)
-2
0
2
4
6
Spike (MLE)
MUA (OLE)
Spike (MLE)
MUA (OLE)
Spike (OLE)

Figure 3

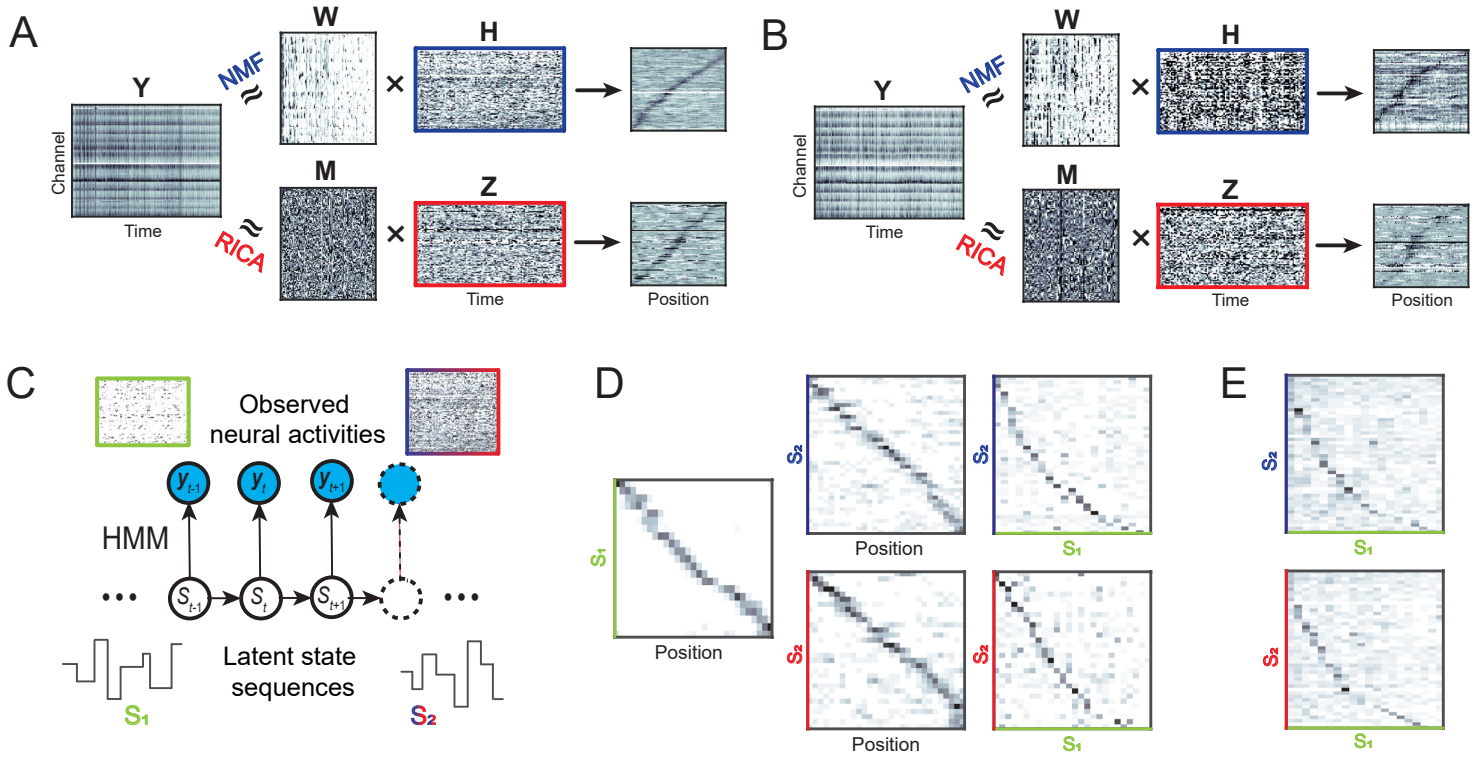
A
Y
Channel
Time
NMF
W
H
RICA
M
Z
Time
Position
B
Y
Channel
Time
NMF
W
H
RICA
M
Z
Time
Position
C
Observed
neural activities
HMM
Latent state
sequences
S1
S2
D
Position
Position
Position
E

Figure 4

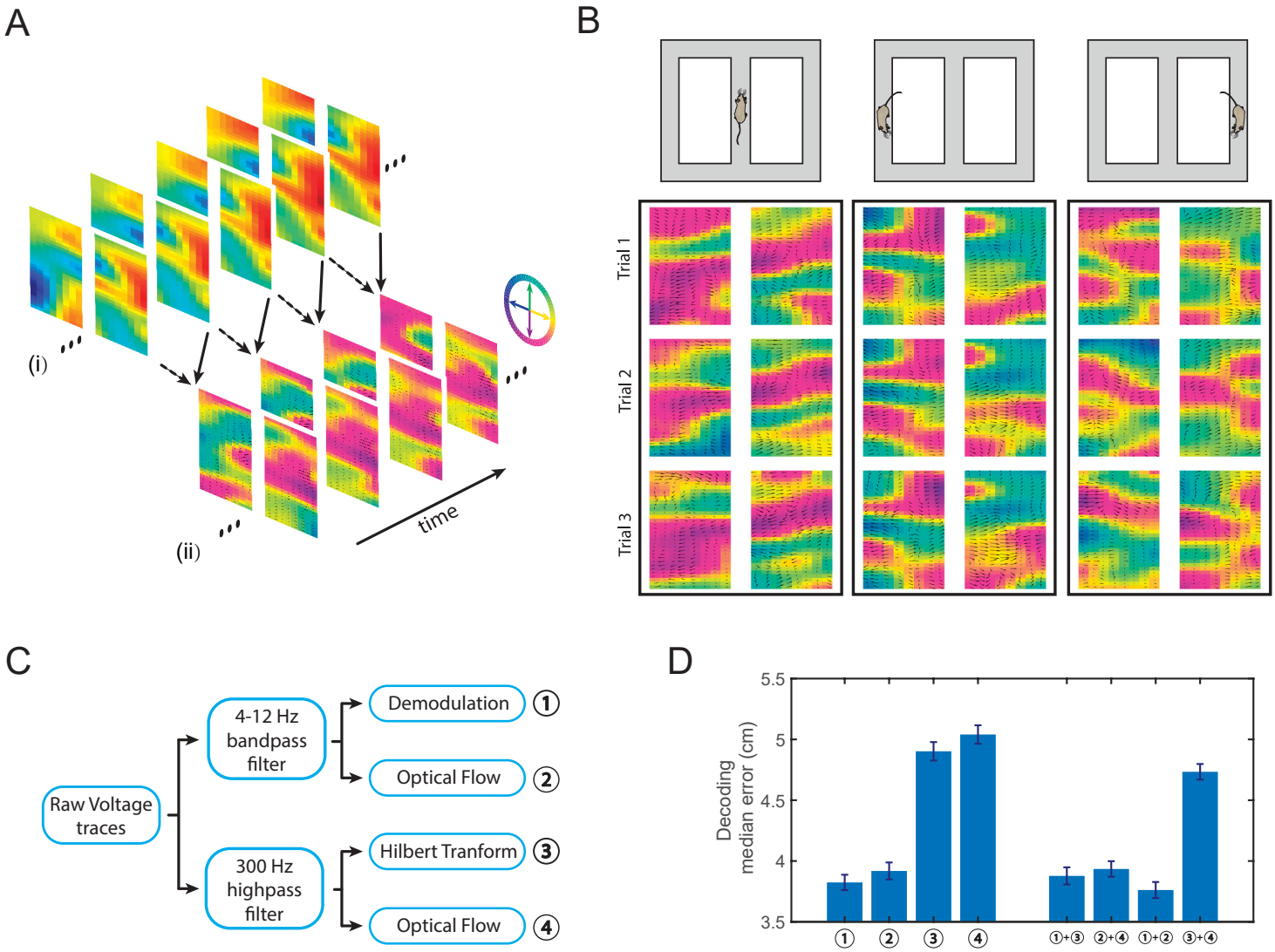
A
(i)
(ii)
time
B
Trial 1
Trial 2
Trial 3
C
Raw Voltage traces
4-12 Hz bandpass filter
300 Hz highpass filter
Demodulation ①
Optical Flow ②
Hilbert Tranform ③
Optical Flow ④
D
Decoding median error (cm)
5.5
5
4.5
4
3.5
① ② ③ ④ ①+③ ②+④ ①+② ③+④

Figure 5

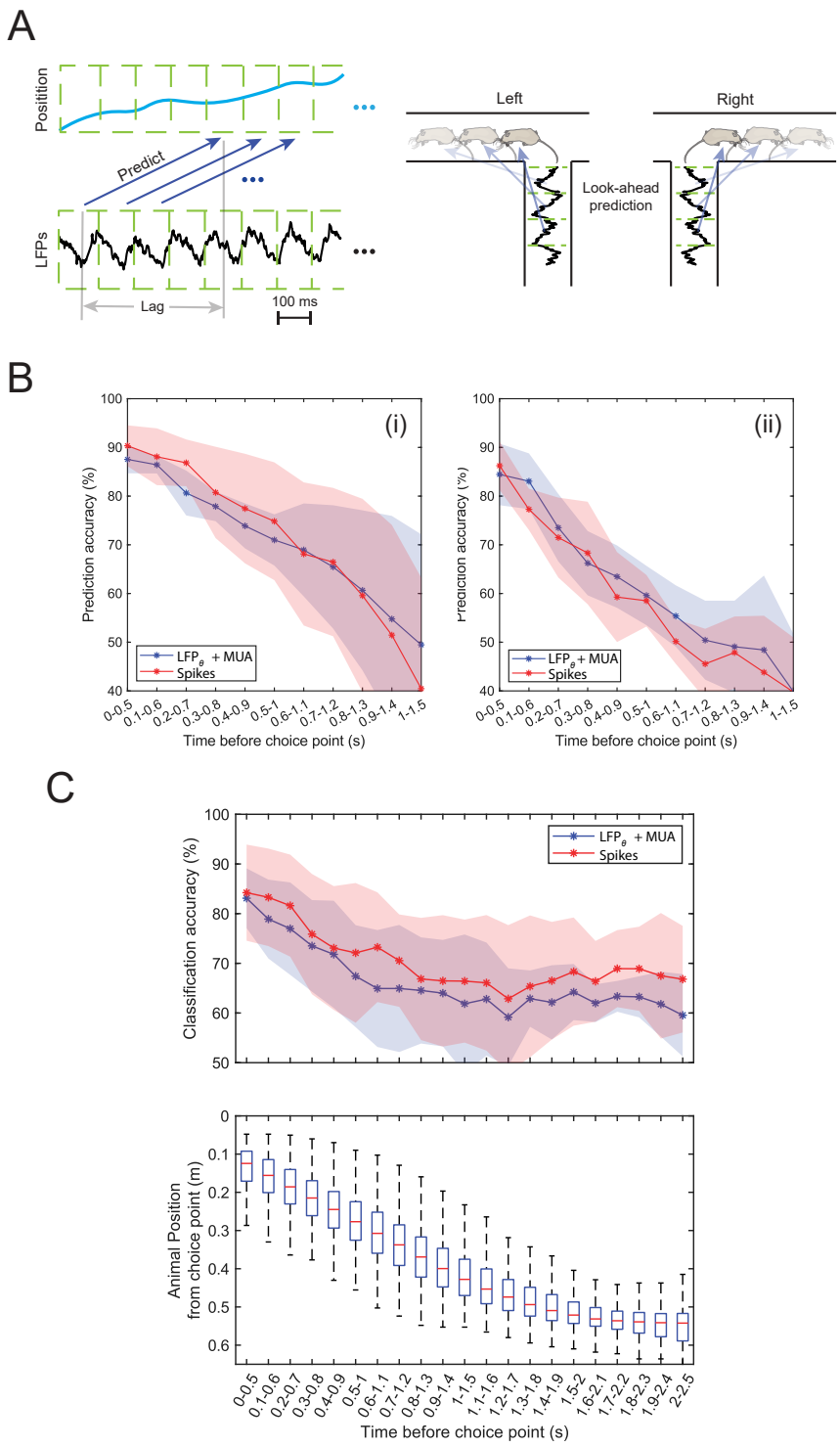
A
Position
Predict
LFPs
Lag
100 ms
Left
Right
Look-ahead prediction
B
(i)
(ii)
Prediction accuracy (%)
LFP$_\theta$ + MUA
Spikes
Time before choice point (s)
C
Classification accuracy (%)
Animal Position from choice point (m)
Time before choice point (s)

Figure 6

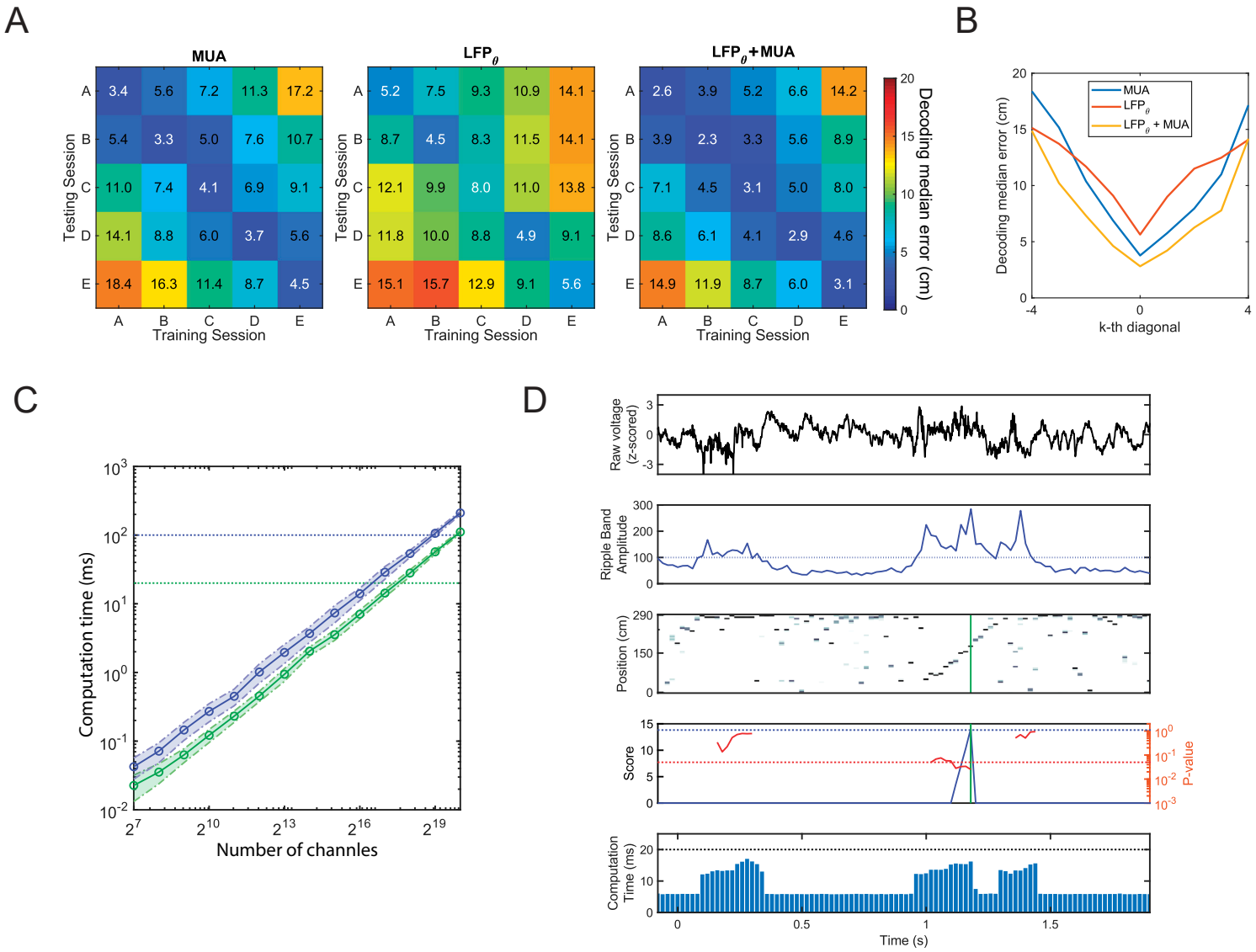
A
MUA
LFP$_\theta$
LFP$_\theta$+MUA
Testing Session
Training Session
A B C D E
3.4 5.6 7.2 11.3 17.2
5.4 3.3 5.0 7.6 10.7
11.0 7.4 4.1 6.9 9.1
14.1 8.8 6.0 3.7 5.6
18.4 16.3 11.4 8.7 4.5
5.2 7.5 9.3 10.9 14.1
8.7 4.5 8.3 11.5 14.1
12.1 9.9 8.0 11.0 13.8
11.8 10.0 8.8 4.9 9.1
15.1 15.7 12.9 9.1 5.6
2.6 3.9 5.2 6.6 14.2
3.9 2.3 3.3 5.6 8.9
7.1 4.5 3.1 5.0 8.0
8.6 6.1 4.1 2.9 4.6
14.9 11.9 8.7 6.0 3.1
Decoding median error (cm)
B
MUA
LFP$_\theta$
LFP$_\theta$ + MUA
Decoding median error (cm)
k-th diagonal
C
Computation time (ms)
Number of channles
D
Raw voltage (z-scored)
Ripple Band Amplitude
Position (cm)
Score
P-value
Computation Time (ms)
Time (s)

Supplemental Information

Ultrafast Readout of Representations from Spatially Distributed Rodent Hippocampal Field Potentials

Liang Cao, Viktor Varga, and Zhe S. Chen*

*Correspondence: zhe.chen@nyulangone.org (Z.S.C.)

Table S1. Related to **Figures 1-6.** Summary of experimental datasets under investigation. Mouse 1 consisted of five sessions, but only four sessions contained well-isolated hippocampal units.

Dataset	Animal	# Session	Environment	# LFP channels	# sorted units
1	Rat 1	1	circular maze (1 m diameter)	64×2 channels	92
2	Rat 1	1	linear track (1.6 m length)	64×2 channels	120
3	Rat 2	1	square T-maze	256×2 channels	223
4	Rat 2	1	linear track	256×2 channels	261
5	Rat 3	1	Open field (120 ×120 cm^2)	32×2 channels	78
6	Mouse 1	5	circular T-maze	64 channels	[56,52,59,46]
	Mouse 2	4	circular T-maze	64 channels	[24,17,12,24]

Table S2. Related to **Figures 1-6.** Summary and comparison of clustered spike-based and LFP-based decoding strategies.

Method	Features	Likelihood	Estimator
Likelihood	clustered spikes	Poisson	MLE
OLE	clustered spikes	Gaussian	linear LS regression
OLE	clustered spikes	Gaussian	sparse VB-ARD linear regression
Likelihood	LFP-based features	Gaussian	MLE
OLE	LFP-based features	Gaussian	linear LS regression
OLE	LFP-based features	Gaussian	sparse VB-ARD linear regression
Bayesian	LFP-based features	Gaussian	Bayesian

Table S3. Related to **Figure 2.** Result comparison between online and offline significance assessment of rat hippocampal memory replay events (Dataset 1).

	Off-line	Online
# detected candidate events	727	672
# significant replay events	129	105
# significant replay events detected by both methods	56	
# significant replay events detected by off-line method only	73	
# significant replay events detected by on-line method only	49	

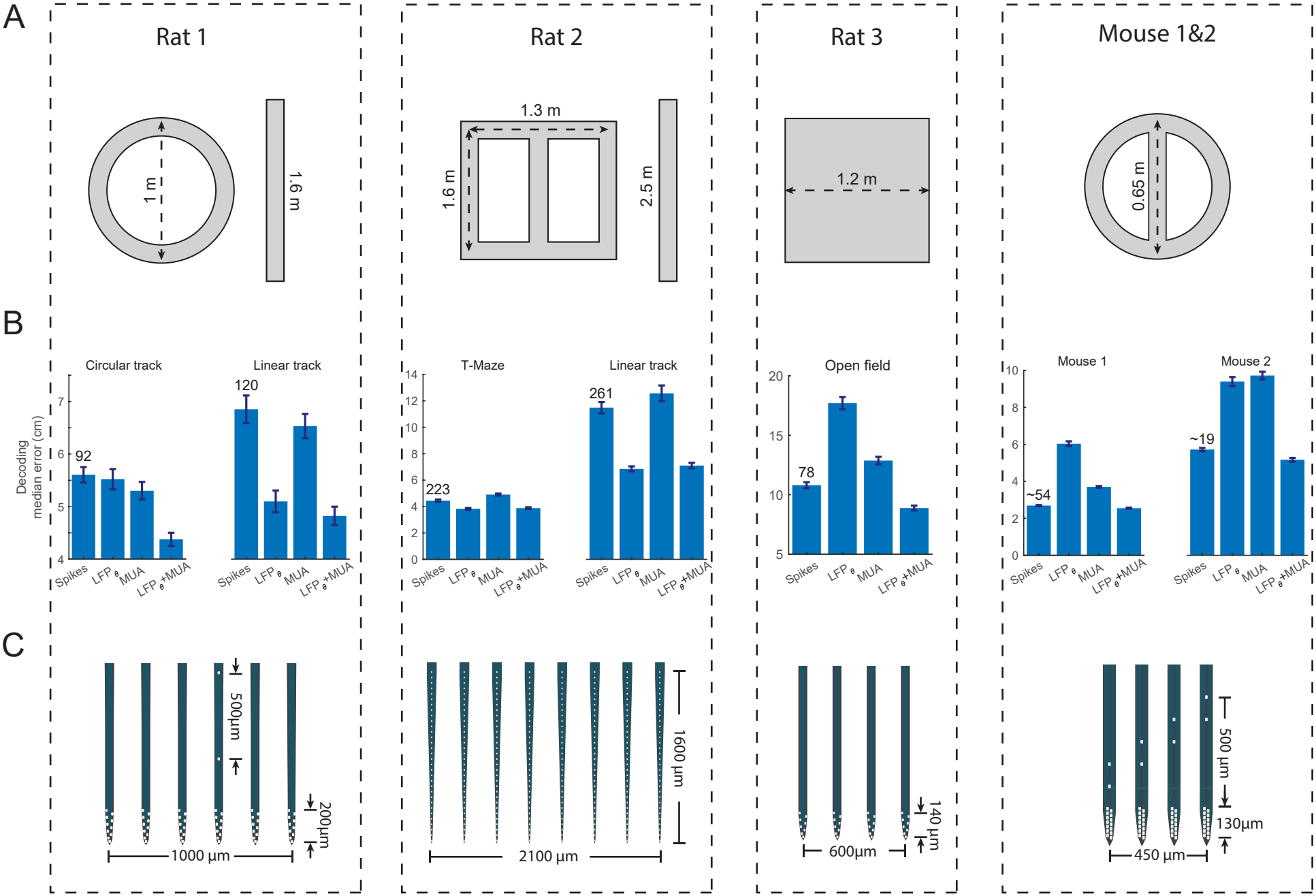

Figure S1. Related to **STAR Methods** and **Figures 1-5**. (**A**) Schematic of four spatial environments using Datasets 1-6. (**B**) Summary of median position decoding error during maze run derived from four different features. Error bar shows the bootstrapped SD. The following default setup was used: 100 ms bin size; OLE decoding method using sparse Bayesian regression. The differing variabilities across animals is largely part of electrode type used. LFP_θ decoding was superior in rat 1 and rat 2 because large numbers of sites across all layers of the hippocampus was used but only a fraction of those were in the pyramidal layer. The number of clustered single units in each session are indicated above the spike bar. (**C**) Configuration of the recording silicon probes used in each dataset.

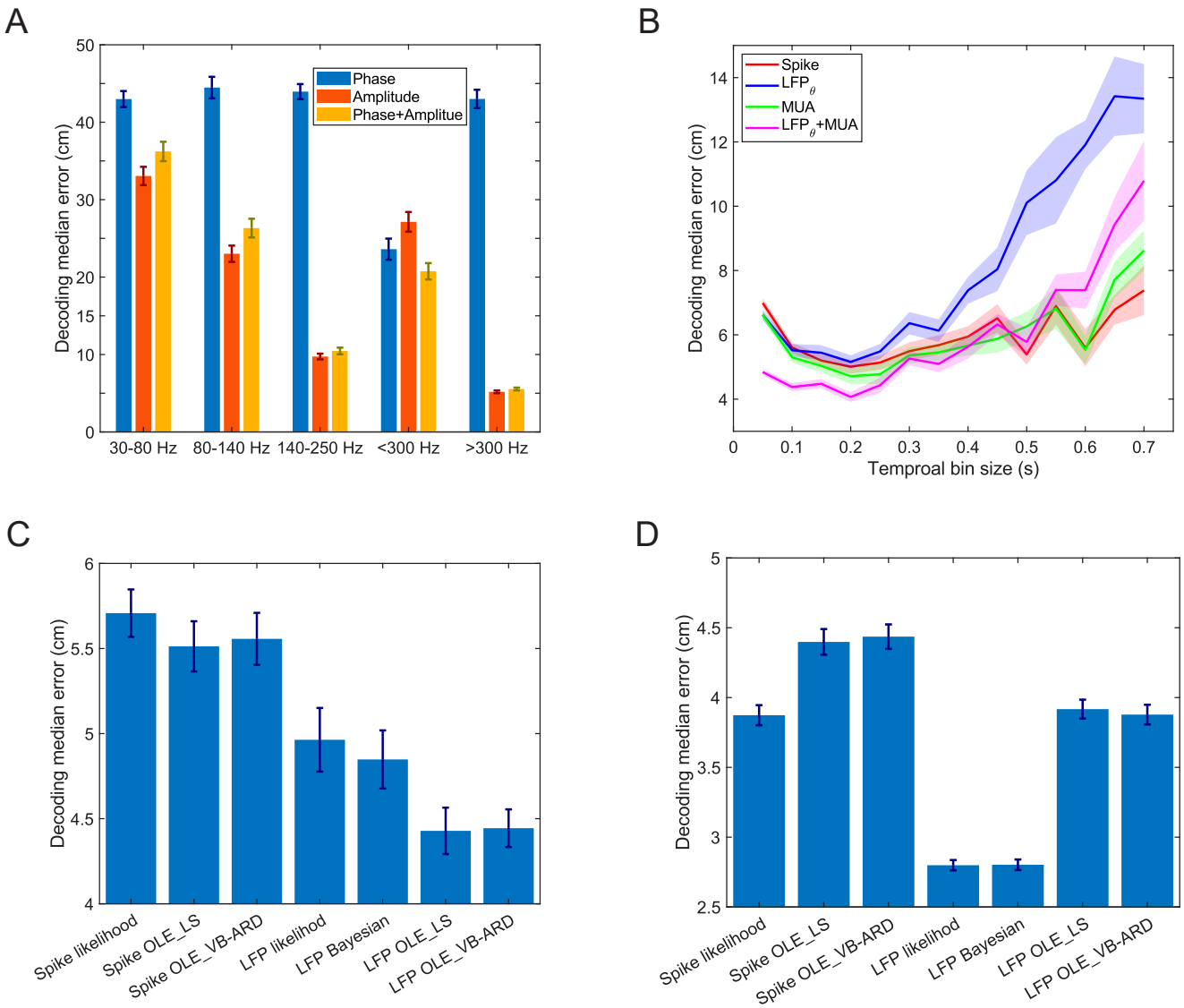

Figure S2. Related to **Figure 1**. Comparison of median position decoding error results derived from different band-pass filtered LFP features (phase, amplitude, phase+amplitude) at (**A**) different frequency bands, (**B**) different temporal bin size, and (**C**) different decoding methods (see **Table S2**; Dataset 1). Shaded area or error bar shows the bootstrapped SD. (**D**) Same as (**C**), except for Dataset 3 using a different configuration of silicon probe.

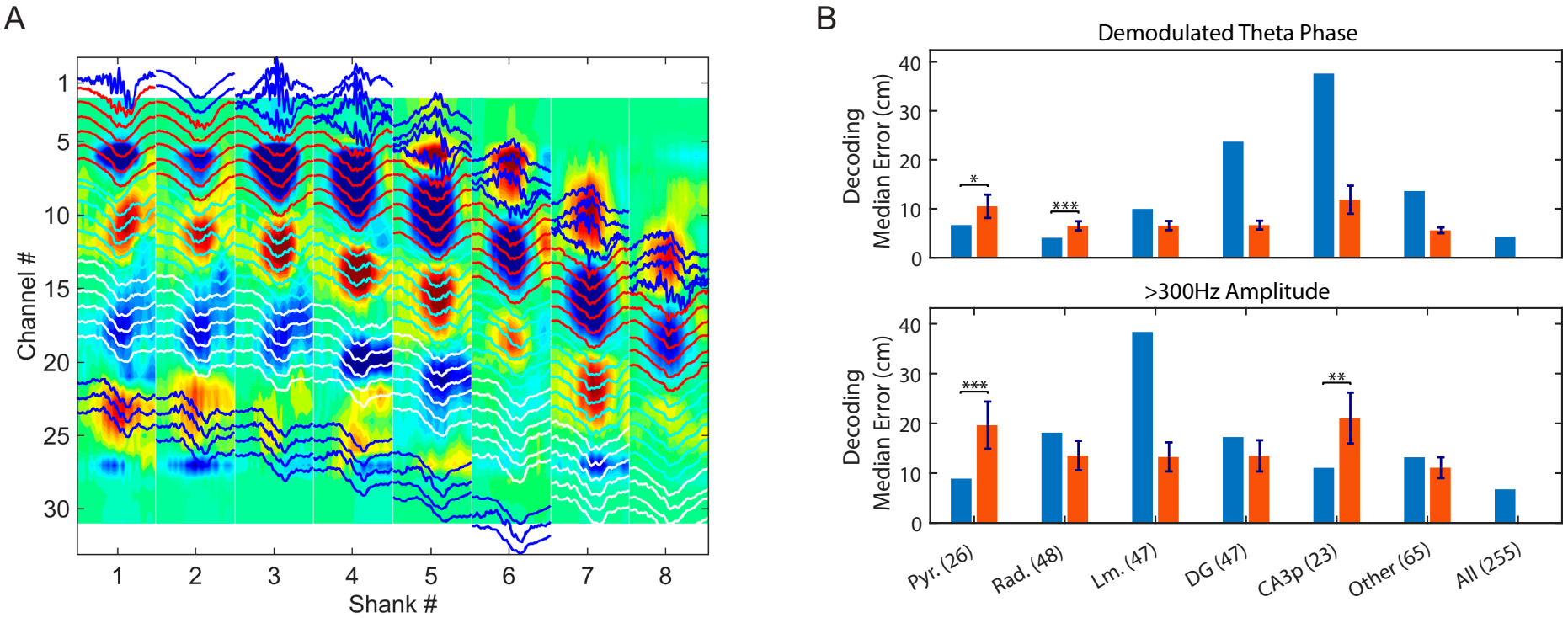

Figure S3. Related to **Figure 1**. (**A**) Current source density (CSD) analysis revealed distinct hippocampal LFP sinks and sources in different anatomical layers (256 channels, 8 shanks, Dataset 3). (**B**) Demodulated LFP_θ (*top*) and MUA (*bottom*) median position decoding error using recording sites in different layers (*blue*) compared to median position decoding error (error bar: SD) derived from 1,000 random selections of matched number of recording sites (red). (Pyr: stratum pyramidale; Rad: stratum radiatum; Lm: stratum lacunosum moleculare; DG: dental gyrus; CA3p: CA3 pyramidal layer). The number inside parentheses indicates the channel count within that layer/region. CA1 layers with changing layer-by-layer theta phase shift gave best position decoding by LFP_θ decoding strategy, while MUA was most effective in CA1 and CA3 pyramidal layer.

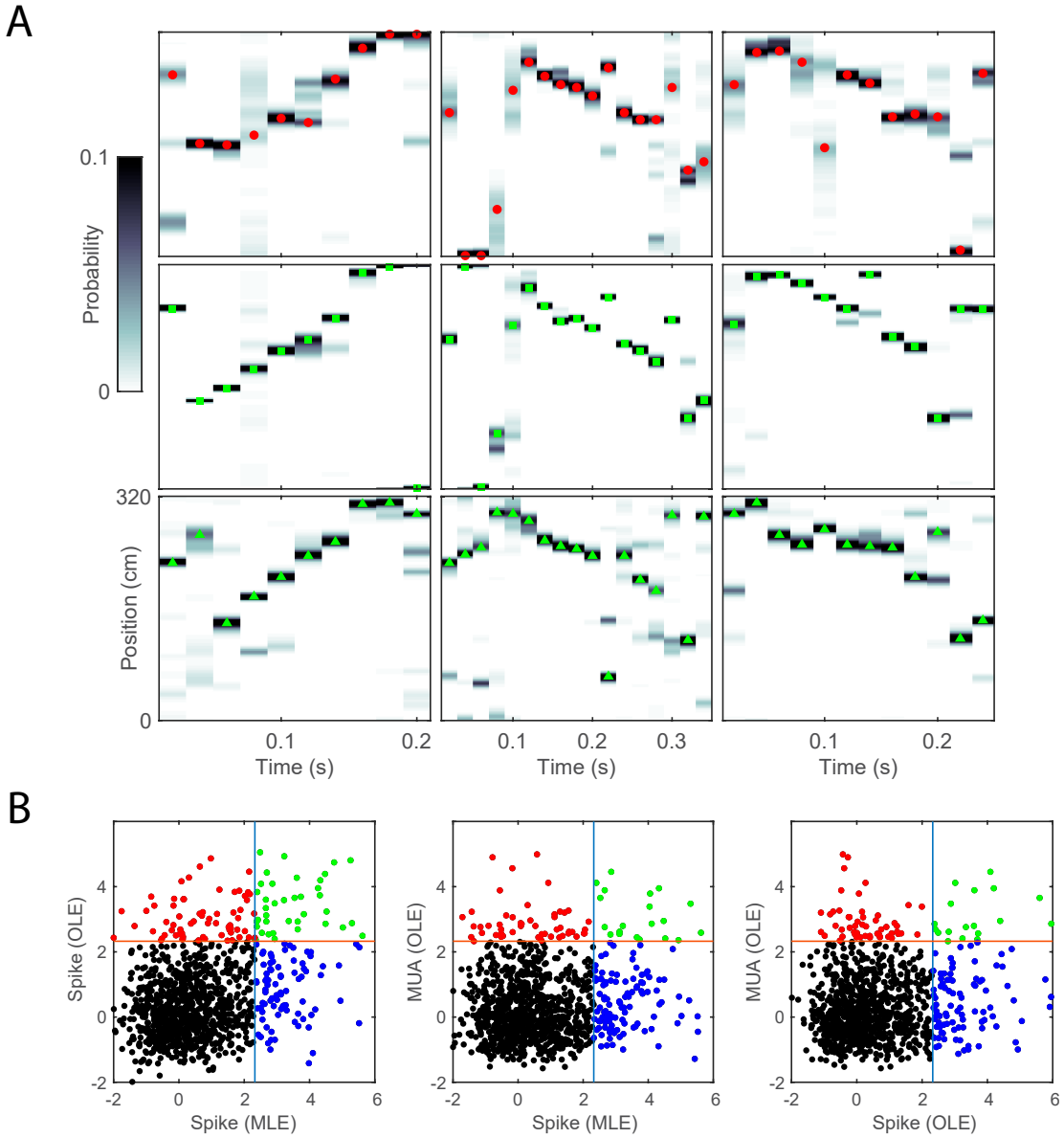

Figure S4. Related to **Figure 2**. (**A**) Examples of decoded ripple-replay contents derived from clustered spikes and MUA features in post-run sleep (Datasets 2). (**B**) Comparison of detection statistics of hippocampal memory replay candidates in awake and NREM ripples (n=1,038 candidate events) derived from spikes and MUA features.

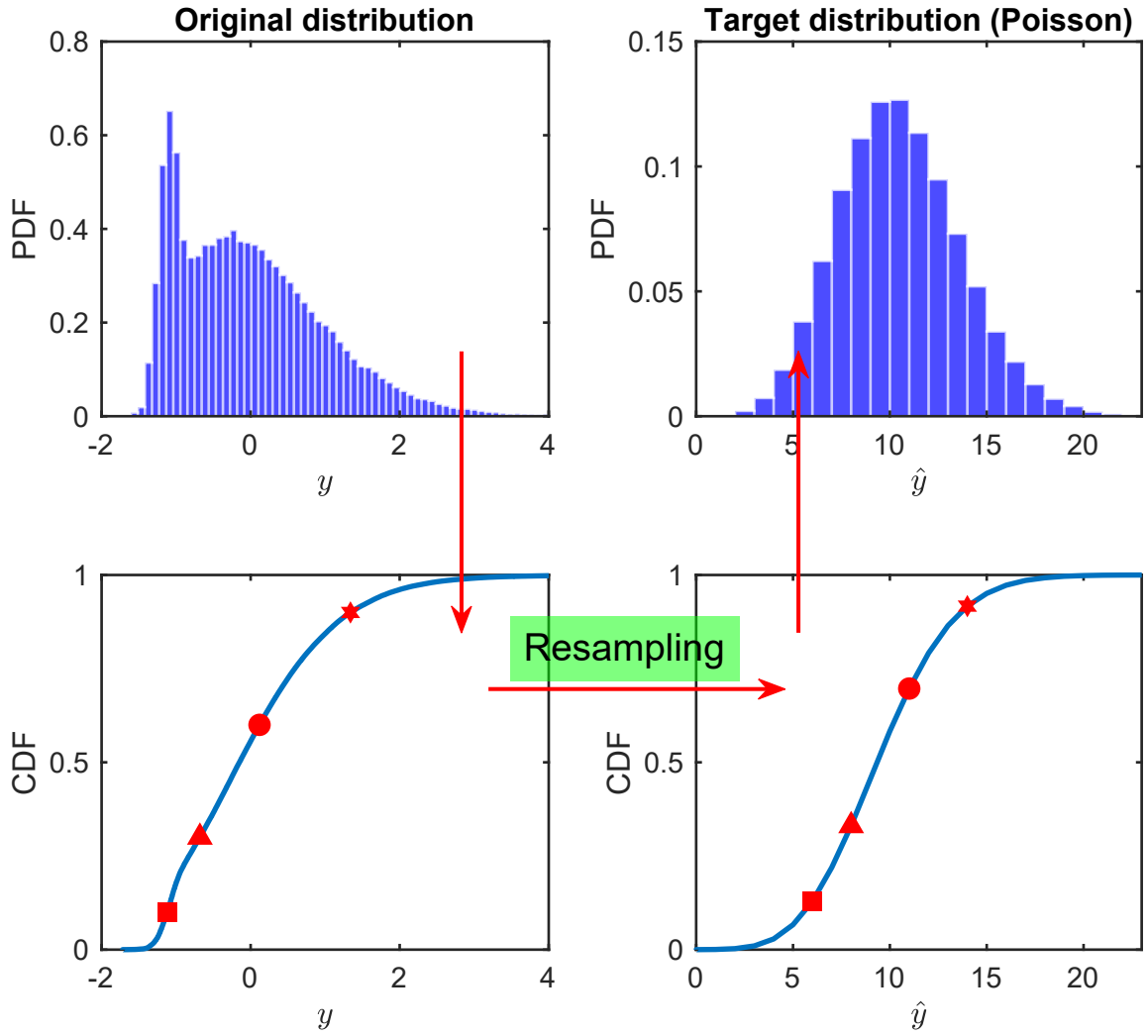

Figure S5. Related to **Figure 3**. Schematic procedure of resampling to rescale the Z-scored real-valued observations y (from an empirical distribution) to nonnegative count observations $\hat{y}$ (from a target Poisson distribution with mean statistic of 10). The red arrows indicate the conceptual procedure. Note that the order statistics remained unchanged between two cumulative distributed function (CDF) curves.

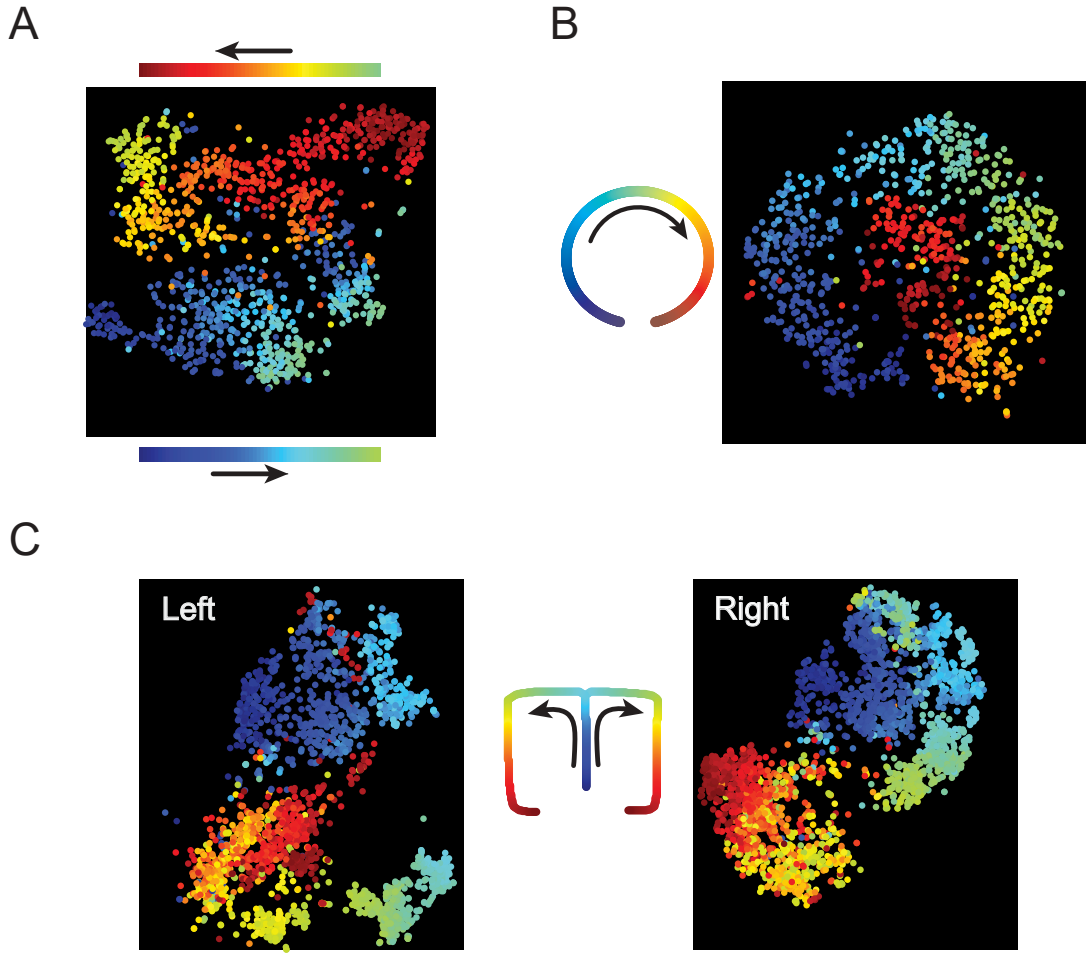

Figure S6. Related to **Figure 3**. Dimensionality reduction of multi-site recorded MUA features during track running, produced by t-distributed stochastic neighbor embedding (t-SNE) algorithm. Each dot was color-coded in relation to the animal's position on the track. Two multi-site MUA feature patterns were similar if they were close in the two-dimensional embedding space. (**A**) For the circular track (Dataset 1), we recovered a continuous trajectory pattern in the embedding space. (**B**) For the linear track (Dataset 2), we recovered direction-specific trajectory pattern in the embedding space. (**C**) For the T-maze (Dataset 3), we recovered distinct clustered patterns, corresponding to L and R turns, in the embedding space.

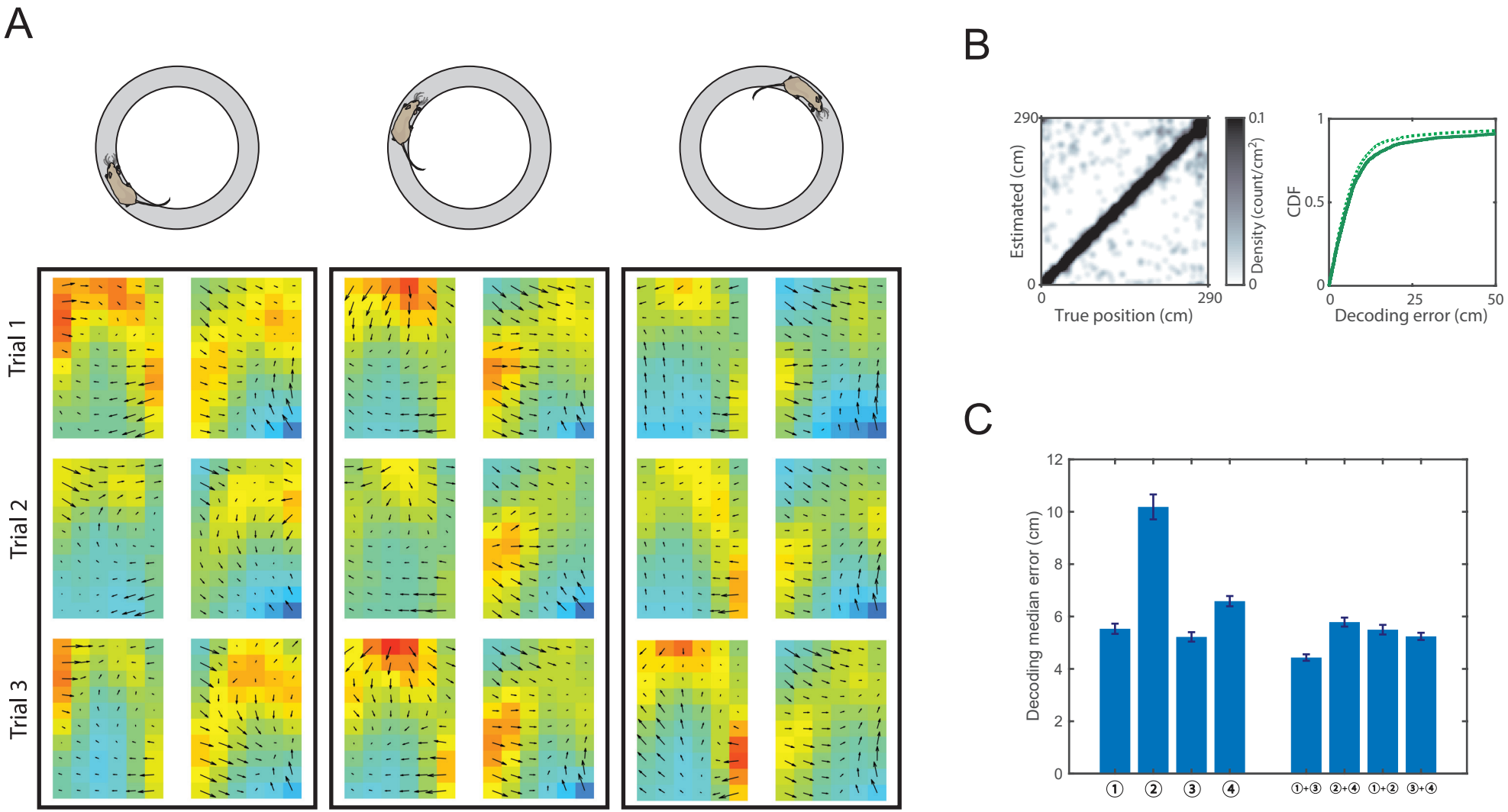

Figure S7. Related to **Figure 4**. (**A**) Optical flow estimated from MUA features (temporal bin size: 100 ms) showed position-dependent patterns on a circular track (Dataset 1). The vector field patterns showed trial-by-trial consistency in three representative trials. See also **Movie S3**. (**B**) Histograms and error CDF curves (solid line) of cross-validated decoding errors based on optical flow of MUA features during run periods (Dataset 1). In the CDF curve, results derived from MUA (dotted line, same as **Figure 1B**) are shown for comparison. (**C**) Comparison of median position decoding error in run behavior derived from different hippocampal LFP spatiotemporal features (the numbers ① ② ③ ④ refer to the same spatiotemporal feature label as Figure 4) and their combinations (Dataset 1). Error bar shows the bootstrapped SD.

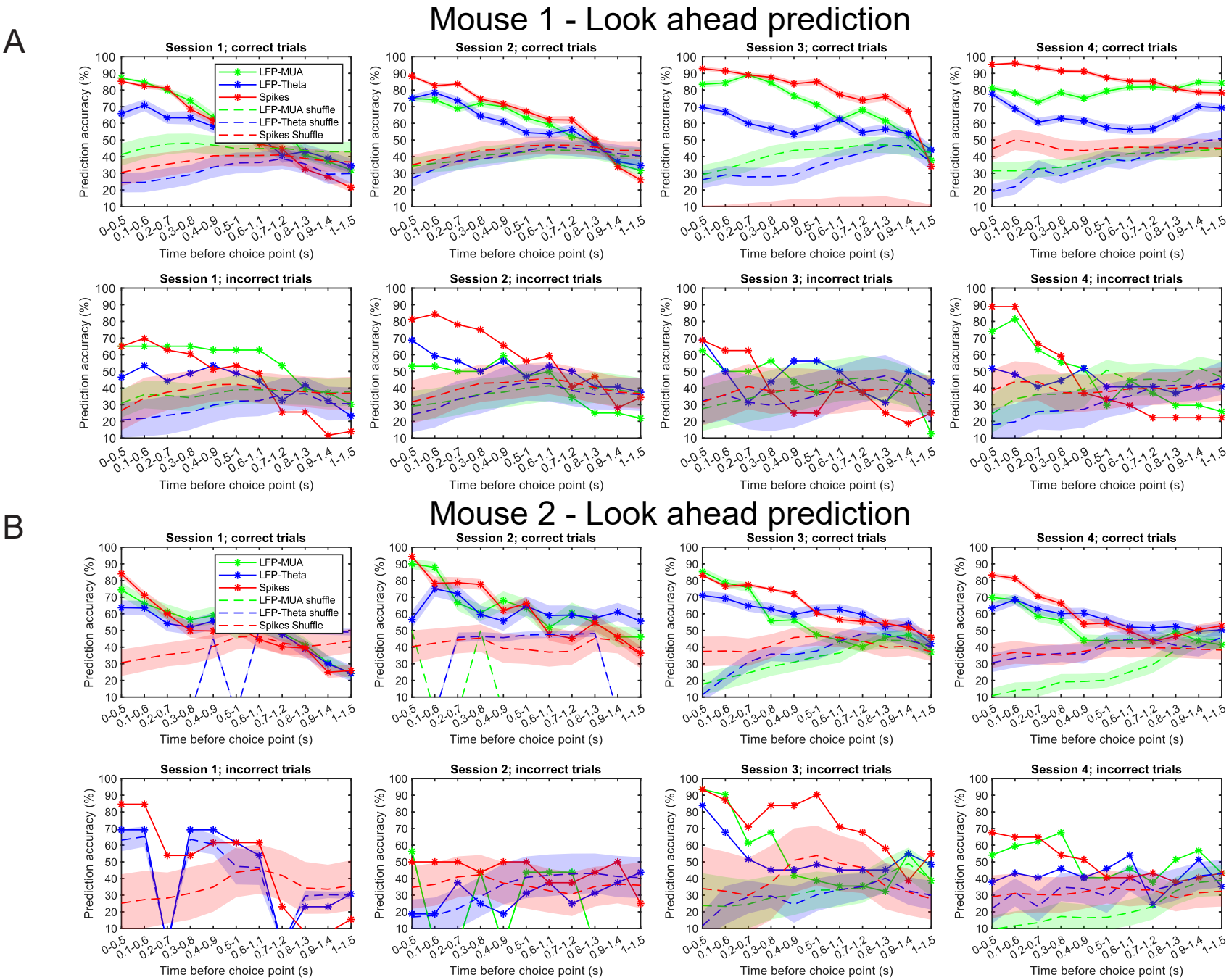

Figure S8. Related to **Figure 5**. Comparison of discrimination accuracy in prospective position decoding (L vs. R arm) derived from clustered spikes and joint (MUA+LFP_θ) for both correct and error trials. Results of four sessions are shown for each mouse (Dataset 6). In each session, we ran 1,000 Monte Carlo runs to compute the mean and SD statistics of 10-fold cross-validation for correct and incorrect trials. Shuffled statistics were also computed for each method and shaded area represents the SD derived from 1,000 random samples. (**A**) mouse 1. (**B**) mouse 2.

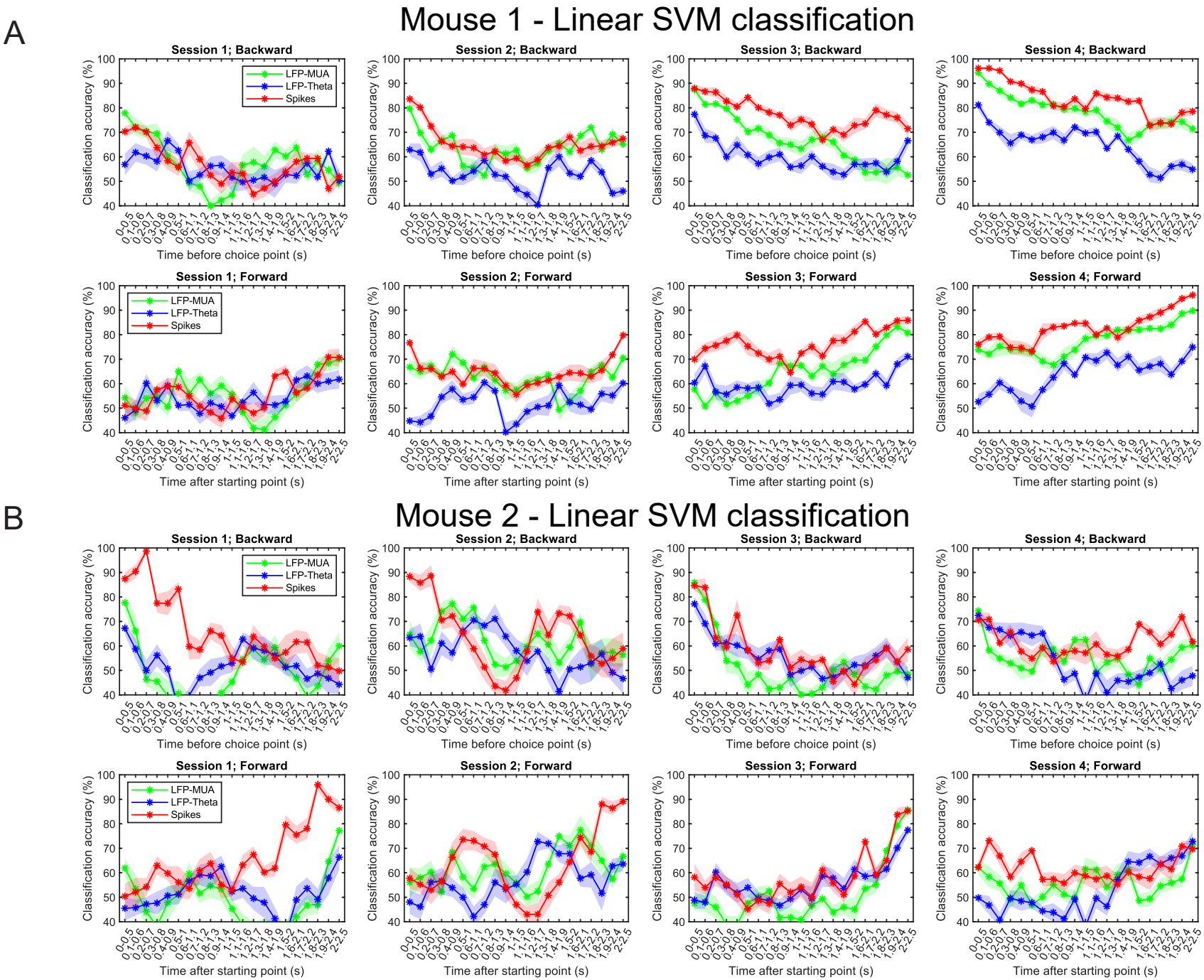

Figure S9. Related to **Figure 5**. Comparison of linear SVM decoding accuracy (L vs. R arm) derived from clustered spike and joint (MUA+LFP$_\theta$) features for correct trials only. Results of four run sessions are shown for each mouse (Dataset 6), in both backward (*top row*) and forward (*bottom row*) directions. In each session, we ran 1,000 Monte Carlo runs to compute the mean and SD statistics of 10-fold cross-validation for correct trials. (**A**) mouse 1. (**B**) mouse 2.

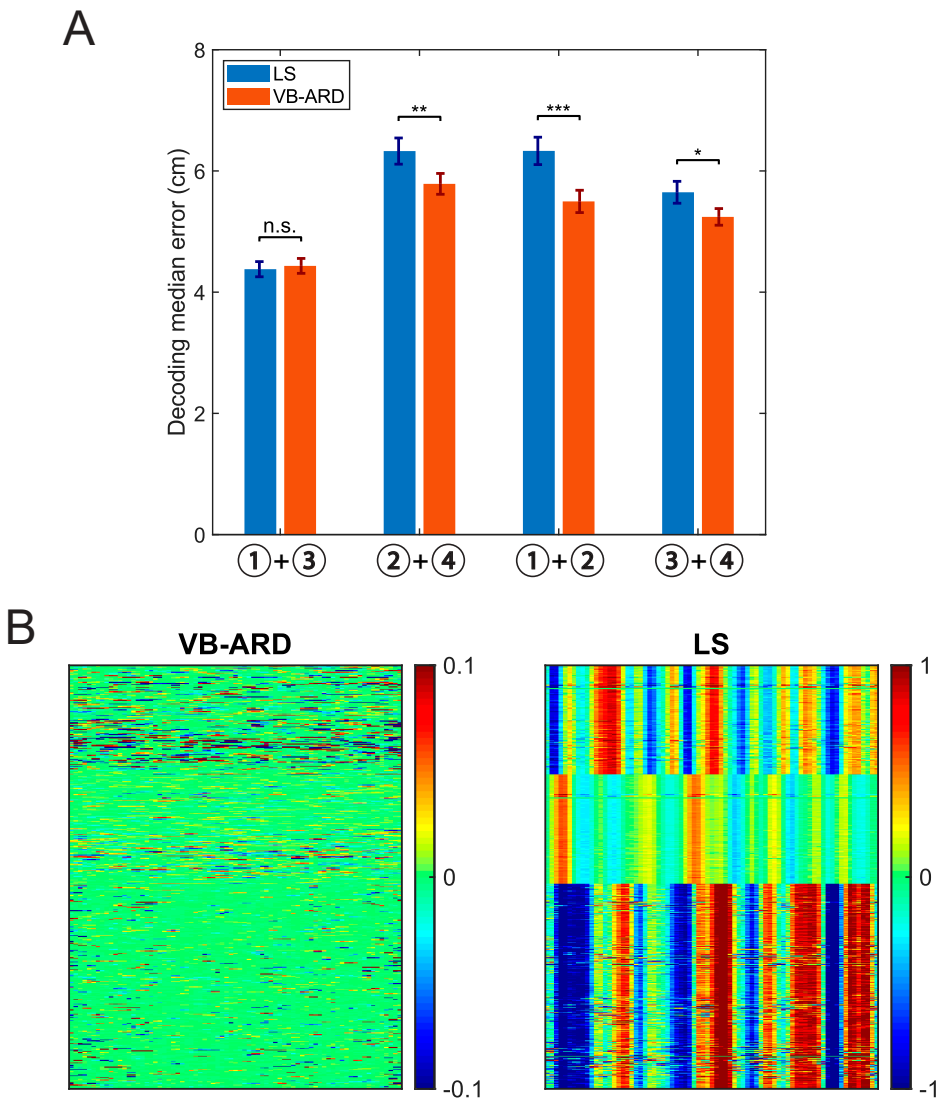

Figure S10. Related to **Figure 1**. (**A**) Comparison of median decoding error results (Dataset 1) between methods using standard least-squared (LS, blue) and sparse VB-ARD (red) regression while testing different combinations of LFP-based features (①: demodulated LFP theta power and phase; ②: LFP-optical flow using 4-12 Hz band; ③: MUA at >300 Hz band; ④: MUA-optical flow at >300 Hz band). *, P<0.05; **, P<0.01; *** P<0.001, rank-sum test. Error bar shows the bootstrapped SD. (**B**) Comparison of the mapping *V* between the VB-ARD (*left*) and LS (*right*) estimators used in the OLE method ("①+②" LFP features combination). The weight coefficients learned from the VB-ARD estimator were sparse.

Supplementary movie legends

Movie 1. Related to **Figure 1.** Demonstration of Bayesian filter (likelihood plus a temporal prior) decoding in an open field environment (Dataset 5) based on clustered spikes, LFP_θ, MUA, joint (LFP_θ+MUA) features, and combining all features. Video frame: 3.3 Hz.

Movie 2. Related to **Figure 5.** Demonstration of location-tuned spatiotemporal patterns in 512-channel rat hippocampal LFP signals filtered at 4-12 Hz (Dataset 3). Animal's actual position (grey) and decoded position (blue) are shown. The 2D vector field illustrates the optical flow patterns across two Buzsaki256 probes. Background was color coded according to the arrow direction. Video frame rate: 10 Hz.

Movie 3. Related to **Figure 5.** Demonstration of location-tuned spatiotemporal patterns in 120-channel rat hippocampal MUA features while running in a circular maze (Dataset 1). Animal's actual position (grey) and decoded position (blue) are shown. The 2D vector field illustrates the optical flow patterns across two Buzsaki64SPL probes (6×10 layout). Background shows the MUA amplitude (warm color represents high value). Video frame rate: 10 Hz.